2018 RMZ M&G Vol 65 No 4

RMZ

MATERIALS and GEOENVIRONMENT

MATERIALI in GEOOKOLJE

RMZ – M&G, **Vol. 65**, No. 4
pp. 167–218 (2018)

Ljubljana, December 2018

RMZ – Materials and Geoenvironment
RMZ – Materiali in geookolje
ISSN 1408-7073

Old title/Star naslov
Mining and Metallurgy Quarterly/Rudarsko-metalurški zbornik
ISSN 0035-9645, 1952–1997

Published by/Izdajatelj
Faculty of Natural Sciences and Engineering, University of Ljubljana/
Naravoslovnotehniška fakulteta, Univerza v Ljubljani

Associated Publisher/Soizdajatelj
Institute for Mining, Geotechnology and Environment, Ljubljana/
Inštitut za rudarstvo, geotehnologijo in okolje
Velenje Coal Mine/Premogovnik Velenje
Slovenian Chamber of Engineers/Inženirska zbornica Slovenije

Editorial Office/Uredništvo
Technical editors/Tehnična urednika Teja Čeru and Jože Žarn
Secretary/Tajnica Nives Vukič

Editorial Address/Naslov uredništva
RMZ – Materials and Geoenvironment
Aškerčeva cesta 12, p. p. 312
1001 Ljubljana, Slovenija
Tel.: +386 (0)1 470 46 10
Fax.: +386 (0)1 470 45 60
E-mail: rmz-mg@ntf.uni-lj.si

Published/Izhajanje
4 issues per year/4 številke letno

Partly funded by Ministry of Education, Science and Sport of Republic of Slovenia./Pri financiranju revije sodeluje Ministrstvo za izobraževanje, znanost in šport Republike Slovenije.

Articles published in Journal "RMZ M&G" are indexed in international secondary periodicals and databases:/Članki, objavljeni v periodični publikaciji „RMZ M&G", so indeksirani v mednarodnih sekundarnih virih:
CA SEARCH® – Chemical Abstracts®, METADEX®, GeoRef.

Annual subscription for individuals in Slovenia: 20 EUR, for institutions: 30 EUR. Annual subscription for the rest of the world: 30 EUR, for institutions: 50 EUR/Letna naročnina za posameznike v Sloveniji: 20 EUR, za inštitucije: 30 EUR. Letna naročnina za tujino: 30 EUR, inštitucije: 50 EUR

Transaction account/Tekoči račun
Nova Ljubljanska banka, d. d., Ljubljana: UJP 01100-6030708186

VAT identification number/Davčna številka
24405388

Online Journal/Elektronska revija
www.rmz-mg.com
www.degruyter.com/view/j/rmzmag

Table of Contents

Kazalo

Historical Review

More than 90 years have passed since the University Ljubljana in Slovenia was founded in 1919. Technical fields were united in the School of Engineering that included the Geologic and Mining Division, while the Metallurgy Division was established only in 1939. Today, the Departments of Geology, Mining and Geotechnology, Materials and Metallurgy are all part of the Faculty of Natural Sciences and Engineering, University of Ljubljana.

Before World War II, the members of the Mining Section together with the Association of Yugoslav Mining and Metallurgy Engineers began to publish the summaries of their research and studies in their technical periodical Rudarski zbornik (Mining Proceedings). Three volumes of Rudarski zbornik (1937, 1938 and 1939) were published. The War interrupted the publication and it was not until 1952 that the first issue of the new journal Rudarsko-metalurški zbornik – RMZ (Mining and Metallurgy Quarterly) was published by the Division of Mining and Metallurgy, University of Ljubljana. Today, the journal is regularly published quarterly. RMZ – M&G is co-issued and co-financed by the Faculty of Natural Sciences and Engineering Ljubljana, the Institute for Mining, Geotechnology and Environment Ljubljana, and the Velenje Coal Mine. In addition, it is partly funded by the Ministry of Education, Science and Sport of Slovenia.

During the meeting of the Advisory and the Editorial Board on May 22, 1998, Rudarsko-metalurški zbornik was renamed into "RMZ – Materials and Geoenvironment (RMZ – Materiali in Geookolje)" or shortly RMZ – M&G. RMZ – M&G is managed by an advisory and international editorial board and is exchanged with other world-known periodicals. All the papers submitted to the RMZ – M&G undergoes the course of the peer-review process.

RMZ – M&G is the only scientific and professional periodical in Slovenia which has been published in the same form for 60 years. It incorporates the scientific and professional topics on geology, mining, geotechnology, materials and metallurgy. In the year 2013, the Editorial Board decided to modernize the journal's format.

A wide range of topics on geosciences are welcome to be published in the RMZ – Materials and Geoenvironment. Research results in geology, hydrogeology, mining, geotechnology, materials, metallurgy, natural and anthropogenic pollution of environment, biogeochemistry are the proposed fields of work which the journal will handle.

Editor-in-Chief

Zgodovinski pregled

Že več kot 90 let je minilo od ustanovitve Univerze v Ljubljani leta 1919. Tehnične stroke so se združile v Tehniški visoki šoli, ki sta jo sestavljala oddelka za geologijo in rudarstvo, medtem ko je bil oddelek za metalurgijo ustanovljen leta 1939. Danes oddelki za geologijo, rudarstvo in geotehnologijo ter materiale in metalurgijo delujejo v sklopu Naravoslovnotehniške fakultete Univerze v Ljubljani.

Pred 2. svetovno vojno so člani rudarske sekcije skupaj z Združenjem jugoslovanskih inženirjev rudarstva in metalurgije začeli izdajanje povzetkov njihovega raziskovalnega dela v Rudarskem zborniku. Izšli so trije letniki zbornika (1937, 1938 in 1939). Vojna je prekinila izdajanje zbornika vse do leta 1952, ko je izšel prvi letnik nove revije Rudarsko-metalurški zbornik – RMZ v izdaji odsekov za rudarstvo in metalurgijo Univerze v Ljubljani. Danes revija izhaja štirikrat letno. RMZ – M&G izdajajo in financirajo Naravoslovnotehniška fakulteta v Ljubljani, Inštitut za rudarstvo, geotehnologijo in okolje ter Premogovnik Velenje. Prav tako izdajo revije financira Ministrstvo za izobraževanje, znanost in šport.

Na seji izdajateljskega sveta in uredniškega odbora je bilo 22. maja 1998 sklenjeno, da se Rudarsko-metalurški zbornik preimenuje v RMZ – Materiali in geookolje (RMZ – Materials and Geoenvironment) ali skrajšano RMZ – M&G. Revijo RMZ – M&G upravljata izdajateljski svet in mednarodni uredniški odbor. Revija je vključena v mednarodno izmenjavo svetovno znanih publikacij. Vsi članki so podvrženi recenzijskemu postopku.

RMZ – M&G je edina strokovno-znanstvena revija v Sloveniji, ki izhaja v nespremenjeni obliki že 60 let. Združuje področja geologije, rudarstva, geotehnologije, materialov in metalurgije. Uredniški odbor je leta 2013 sklenil, da posodobi obliko revije.

Za objavo v reviji RMZ – Materiali in geookolje so dobrodošli tudi prispevki s širokega področja geoznanosti, kot so: geologija, hidrologija, rudarstvo, geotehnologija, materiali, metalurgija, onesnaževanje okolja in biokemija.

Glavni urednik

Original scientific paper

Received: May 17, 2018
Accepted: Nov 30, 2018
DOI 10.2478/rmzmag-2019-0005

Decarburization of the Carbon Steel C45 During Annealing in Air

Razogljičenje ogljikovega jekla C45 med žarjenjem na zraku

Matija Zorc[1], Aleš Nagode[1], Milan Bizjak[1], Borut Zorc[1,2]

[1] Univerza v Ljubljani, Naravoslovnotehniška fakulteta, Aškerčeva 12, Ljubljana, Slovenia; matija.zorc@gmail.com; ales.nagode@omm.ntf.uni-lj.si ; milan.bizjak@omm.ntf.uni-lj.si

[2] Inštitut za varilstvo, Ptujska 19, Ljubljana, Slovenia; borut.zorc@i-var.si

* Inštitut za varilstvo, Ptujska 19, Ljubljana, Slovenia; borut.zorc@i-var.si

Abstract

In production it is necessary to achieve conditions that lead to the minimum decarburization of a steel product's surfaces. In this study, the hypo-eutectoid carbon steel C45 was annealed in air in the temperature range T_a = 600–1100 °C. The annealing times were between t_a = ½ h and t_a = 2 h. Different decarburizations occurred in different microstructures: ferrite–pearlite (T_a = 600 °C and 700 °C, $T_a < A_{C1}$, no visible decarburization); ferrite–austenite (T_a = 760 °C, $A_{C1} < Ta < A_{C3}$, visible decarburization); austenite at the beginning, ferrite–austenite after the incubation period (Ta = 850 °C, $A_{C3} < T_a < 912$ °C, visible decarburization); and austenite (T_a = 950 °C and 1100 °C, $T_a > 912$ °C, visible decarburization and overheating of steel). The edges were more prone to decarburization and to overheating. Stress relieving, normalizing and annealing before quenching of the steel C45 can be carried out in air.

Key words: annealing, hypo-eutectoid steel, air, oxidation, decarburization

Povzetek

Tehnološko je nujno potrebno dosegati pogoje, ki vodijo k minimalnemu razogljičenju površin jeklenega izdelka. V tej študiji smo podevtektoidno ogljikovo jeklo C45 žarili na zraku, v temperaturnem območju od T_a = 600 do 1100 ° C. Čas žarjenja t_a je bil med ½ ure in 2 urama. Različne stopnje razogljičenja so nastajale v različnih mikrostrukturah: ferit-perlit (T_a = 600 ° C in 700 ° C, $T_a < A_{C1}$, brez vidnega razogljičenja); ferit-avstenit (T_a = 760 ° C, $A_{C1} < T_a < A_{C3}$, vidno razogljičenje); avstenit na začetku, ferit-avstenit po inkubacijski dobi (T_a = 850 ° C, $A_{C3} < T_a$ <912 ° C, vidno razogljičenje); in v avstenitu (T_a = 950 ° C in 1100 ° C, $T_a > 912$ ° C, vidno razogljičenje in pregretje jekla). Robovi so bili bolj nagnjeni k razogljičenju in pregretju. Žarjenje za odpravo napetosti, normalizacijo in žarjenje pred kaljenjem jekla C45 lahko glede na izsledke te študije izvajamo na zraku.

Ključne besede: žarjenje, podevtektoidno jeklo, zrak, oksidacija, razogljičenje

Introduction

The oxidation and decarburization of the steel happen simultaneously during annealing in an oxidising atmosphere. Burning the carbon from the surface creates a difference in the carbon concentrations between the surface and the inner layers of the steel, leading to a constant diffusion of carbon from the inner layers towards the surface. This results in an unwanted, either completely or partially decarburized layer on the surface. In production it is necessary to achieve conditions that lead to the minimum decarburization of a steel product's surfaces. This either involves measures that prevent carbon from burning or annealing conditions under which the oxidation of steel is faster than the diffusion of carbon and therefore decarburization [1–3].

Decarburization is a process in which the carbon content in the surface of steel products decreases during the annealing when the steel is exposed to gases like O_2, CO_2, H_2O and H_2 at elevated temperatures [1–3]. The carbon on the surface of the steel reacts with these gases, producing CO and CO_2 in an oxidizing atmosphere, or CH_4 in a hydrogen atmosphere. Because of these reactions the carbon is able to escape from the steel, creating a surface layer with a lower carbon content. Concurrently, at $T > 570$ °C in an oxidizing atmosphere iron generally oxidizes to form FeO. Decarburization occurs when the chemical potential of the carbon in the atmosphere is lower than the equilibrium carbon potential that is needed to maintain the carbon content on the surface of the annealed steel. Decarburization is therefore a means of achieving the thermodynamic equilibrium between the steel and the atmosphere at the annealing temperature. Since this is not possible, burning of carbon on the surface creates and maintains the concentration gradient of the carbon between the surface and the interior of the steel product. This creates the conditions for the permanent diffusion of carbon from the interior into the surface of the steel. Because of this, longer annealing times mean thicker decarburized layers. Therefore, decarburization is a result of simultaneous oxidation and diffusion processes and is only visible when the diffusion of carbon is faster than the oxidation of the metal [1, 3–7]. There are many factors that affect the kinetics of decarburization [3–6]: the type of atmosphere and its flux, the time and temperature of the annealing, the proportion of carbon and other alloying elements in the steel, the condition of the surface (ground without scale, with scale), the microstructure of steel on the annealing temperature and the shape of the steel product (edges, notches, thin jutting parts and similar). Strong decarburization occurs in the vicinity of the rolled-in scale and in the vicinity of the cracks that were already present prior to the annealing [1,2,6,8].

Depending on the conditions of annealing, decarburization can occur in three forms: as a ferrite surface layer (total decarburization), as a surface layer with a higher ferrite content than the non-decarburized parts (partial decarburization; here the content of ferrite gradually reduces with distance from the surface, to the point where the ferrite content is equal to that in the non-carburized parts) and as a combination of those two with ferrite surface layer and a partially decarburized layer below it [1–9]. A clearly visible partial decarburization with a higher ferrite content is a characteristic of a microstructure that was ferritic–pearlitic or pearlitic prior to annealing, while partial decarburization in quenched and tempered microstructures is not so clearly visible because of the needle-like microstructure [9,10]. A partially decarburized layer in sferoidize-annealed hyper-eutectoid tool steels is visible as a lamellar pearlite [1,9]. Compared to a non-decarburized material, the decarburized layer has a lower hardness (lower wear resistance, easier creation of surface damage and therefore the notch effect), a lower yield strength and tensile strength (possibility of surface-crack initiation because of overloading) and a lower fatigue strength (lower resistance to cyclic loading). In general, a fatigue crack will always be initiated in a ferrite surface layer [1,6]. It is known that in unfavourably oriented ferrite grains in (110) crystal planes even stresses that are lower than the yield strength can create conditions that make dislocation slips possible [11,12]. This means that a surface crack can initiate even when the surface is not damaged and at stresses that are acceptable for construction applications. All this being said, decarburization is

usually considered as being a negative feature. Partial decarburization is, however, recommended in products produced from quenched and tempered steel. In this case the partial decarburization is acceptable as it slightly reduces the surface hardness and therefore increases the ductility and the resistance of the tempered martensite to brittle fracture [10]. In practice it is necessary to achieve conditions that result in the lowest possible decarburization of the surface, whether with procedures that prevent burning of the carbon on the surface or with conditions of annealing at which the oxidation of steel is faster than the carbon diffusion. These kinds of conditions can also be achieved in the air, which is otherwise unfavourable for annealing, but is cost-free.

This article combines theoretical analyses of oxidation with experimental results for the annealing of the hypo-eutectoid steel C45 (EN 10027-1) with a ground surface at different annealing temperatures and times in the air.

Materials and Methods

Research was conducted on non-alloyed, hypo-eutectoid carbon steel C45 with chemical composition as follows: C = 0.43, Si = 0.22, Mn = 0.61, P = 0.034, S = 0.014, Fe: balance, all in wt.%. The chemical composition was determined with an emission spectrometer. Steel's transformation temperatures are A_{C1} = 735 °C and A_{C3} = 785 °C [13]. Suggested hot-working and heat-treatment temperatures are: forging at T = 850–1100 °C, normalization at T = 840–870 °C, quenching from T = 820–860 °C, tempering at T = 530–670 °C, and spheroidizing at T = 650–700 °C [2]. The microstructure of the steel prior to annealing was ferritic–pearlitic.

Annealing took place in the ambient air (humidity and consequently the effect of water vapour was neglected), which means in a gas mixture consisting of 78 vol.% N_2, 21 vol.% O_2 and 1 vol.% of other gases. Annealing temperatures (T_a = 600, 700, 760, 850, 950, 1100; in °C) and annealing times (t_a = ½, 1, 2; in hours) were chosen congruently with the parameters for different types of annealing and hot working. From a metallurgical point of view this means decarburization in different microstructural states: ferrite–pearlite (Ta < A_{C1}), ferrite–austenite (A_{C1} < Ta < A_{C3}), firstly austenite and ferrite–austenite after the incubation period (A_{C3} < T_a < 912 °C) and austenite (T_a > 912 °C).

Samples were cut from a rod with a circular diameter D = 135 mm. They were in a cubic shape with average dimensions 40 × 30 × 17 mm and mass m = 160 g ± 20 g. Prior to annealing, the masses of all the samples were measured and they were put into groups in a way so that the differences between the masses of all three samples that were annealed at the same temperature at different times were within 5 grams of each other. The surfaces of the samples were ground with SiC paper #80 prior to the annealing to obtain a light metallic surface and thus were without any traces of oxides.

Each sample was annealed in a CARBOLITE laboratory electrical resistance furnace with a volume of 22 dm^3 with a static air atmosphere. The furnace has a programmer that allows it to set the temperature and annealing time as well as the heating rate to the annealing temperature. As the atmosphere heats faster than the sample, these temperatures were also controlled using a certified ALMEMO 2590-9 contact thermocouple, which was inserted into the furnace from a hole in the ceiling and was in contact with the sample from the side. Each sample was put in exactly the same place in the furnace (on a fireproof brick in the centre of the furnace). Before they were put in place, both the furnace and fireproof brick were heated to and stabilized at the annealing temperature. This guaranteed the same conditions and as fast as possible heating of each sample to its annealing temperature. The annealing time was being measured from the point when the sample or the control thermometer achieved a temperature of T = T_a – 0.5 °C. During the process the temperature changed in the range T_a – 1°C ≤ T ≤ T_a + 3 °C. After the annealing the samples were cooled out of the furnace in the air.

The decarburization depth was researched with optical microscopy. With this method it is possible to assess the totally decarburized layer (ferrite) and the partially decarburized one (higher content of ferrite than in non-decarburized steel) in the ferritic–pearlitic microstructure. Metallographic samples were wet-ground

with a SiC paper up to #4000, polished with a ¼ μm diamond paste and etched with 3% HNO_3 in ethanol. Decarburization was assessed on the surfaces and edges (cutting area through the middle of the sample on a longer side) that were in contact with the air atmosphere (upper surface and sides). The depth of the visible decarburization was measured in two ways so that the results were sure to be correct. Firstly, a conventional approach on a microscope with a measuring ocular was used (because of the different magnifications, the length between two lines was measured with a micrometre plate), and secondly a computer version of this method was employed.

The surface of samples was ground prior to the annealing, so the effect of the scale on the kinetics of decarburization was nullified. It is a well-known fact that a preliminary scale increases the intensity of decarburization [9].

Results and discussion

Surface oxidation

It is well known that a high temperature and longer annealing times caused a higher degree of surface oxidation. Although the oxidation process of iron and the composition of oxide layer at temperature range from T = 570 do 700 °C are different as at T > 700 °C [14], based on the Fe-O phase diagram is generally accepted that during steady-state annealing in air the oxide layer at T > 570 °C is composed from three layers. At temperatures T > 700 °C, the composition is, regardless of its depth, approximately 95% FeO, 4% Fe_3O_4 and 1% Fe_2O_3 [6,11,14,15]. The formation of different oxides in scale can be simplified according to the following chemical reactions [2,16]:

$$2Fe + 3/2\ O_2 = Fe_2O_3 \quad \text{(a)},$$

$$3Fe + 2\ O_2 = Fe_3O_4 \quad \text{(b)},$$

$$Fe + 1/2\ O_2 = FeO \quad \text{(c)}.$$

In our case most of the scale shattered and fell off the surface during the manipulation of the samples. Therefore, we were unable to accurately measure the thickness of the scales (we could only measure parts of scale on the samples that were annealed at T_a = 1100 °C and t_a = 2 h, whose thickness was more than 1.0 mm). Despite the fact that the oxidation of carbon steels is slower than the oxidation of iron [14], we assumed and simplified that oxidation of the carbon steel C45 is similar to the oxidation of iron, since the C45 steel contains a very small amount of alloying elements. Generally, at temperatures T > 570 °C iron and carbon steel oxidation follows a parabolic law [14,16] (in [15] it is stated that this occurs at T = 700–1000 °C). The thickness of the scale d_{ox} that formed on the surface of the steel C45 was therefore calculated with an equation for iron oxidation [6,15]:

$$d_{ox} = \sqrt{6 \cdot t \cdot e^{\frac{-20392}{T}}}, \text{(cm)} \quad (1),$$

where t is time (s) and T is the absolute annealing temperature (K). **Table 1** shows calculated values of the scale that forms during the annealing of the hypo-eutectoid, non-alloyed steel C45 in air under our experimental annealing conditions. A comparison between our data and the experimental data for the oxidation of steel 55SiCr with 1.51 wt.% Si and 0.70 wt.% Cr shows that the steel 55SiCr oxidizes more slowly [5] [(a) T_a = 750 °C, t_a = 1 h → steel 55SiCr: d_{ox} = 30 μm, equation 1: d_{ox} = 69 μm; (b) T_a = 1100 °C, t_a = 1 h → steel 55SiCr: d_{ox} = 530 μm, equation 1: d_{ox} = 875 μm; (c) T_a = 1100 °C, t_a = 2 h → steel 55SiCr: d_{ox} = no

Table 1. *Calculated scale thickness on the surface of C45 steel after annealing in the air.*

	Annealing time t (s):		
	1800	3600	7200
Temperature T (°C)	**Scale thickness d_{ox} (μm)**		
600	9	12	18
700	29	41	58
760	54	76	107
850	118	168	237
950	249	352	498
1100	619	875	1238

data, equation 1: d_{ox} = 1238 μm], which is a result of the higher silicon content and the added chromium. Taking into account our approximate scale thickness measures after annealing at T_a = 1100 °C and t_a = 2 h, we concluded that equation (1) adequately describes the oxidation of non-alloyed steel C45 during the annealing in air.

Surface decarburization

During the annealing of steel at scale/steel interface a gas mixture of (CO + CO_2) forms in the air by the reactions between carbon from steel and oxygen from air. However, simultaneously the carbon from the steel reacts also with previously formed CO_2 according to Boudouard reaction [2]:

$$2C + O_2 = 2CO \quad \text{(d)},$$

$$C + O_2 = CO_2 \quad \text{(e)},$$

$$C + CO_2 = 2CO \quad \text{(f)}.$$

The stability of CO increases with higher temperature; at pressure p = 1 atm, e.g. the ratio CO/CO_2 = 1 is achieved in a gas mixture at $T \approx 675$ °C, while the ratio $CO/CO_2 = 4$ is achieved at $T \approx 750$ °C [2]. Hence, with increasing temperature the reactions (d) and (f) prevail.

Decarburization only occurs if newly created gases are able to escape from the steel/scale boundary into the atmosphere. This means that the scale has to be permeable to these gases. The scale is permeable because of cracking and porosity. Non-porous scale becomes permeable above the critical thickness $d_{ox} \approx 50$ μm, when the tendency for cracking and peeling of the scale from the steel's surface occurs [11]. Scale with an overcritical thickness will crack because of combination of different phenomena: growing tensile stresses in wüstite (those generated due to local changes in composition of FeO), reduction of plastic deformation ability of scale to conform the steel surface and sufficiently high pressure of carbon oxides (those created during decarburisation) in space between the scale and the steel. So, in the early stage of oxidation, the process of decarburization is suppressed. But when gaseous carbon oxides are free to escape into the atmosphere,

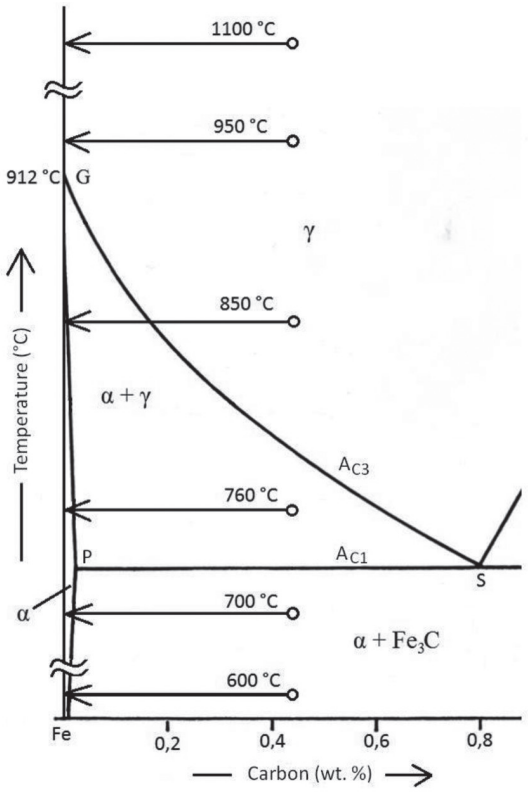

Figure 1: *Microstructural changes for steel with C = 0.43 wt.% due to decarburization (schematically).*

the processes of oxidation and decarburization will happen simultaneously. Decarburization causes the chemical composition and the microstructure of the affected layer of steel to change during the annealing.

For non-alloyed steels the process can be theoretically described with the left part of the Fe–Fe_3C phase diagram, which in the case of our steel with C = 0.43 wt.% is shown in Figure 1, together with all the annealing temperatures. It is not necessary that all the microstructural changes will be seen. Visible decarburization actually occurs only when the decarburization and carbon diffusion in the steel are faster than the oxidation of the steel's surface.

The state of the flat surfaces after the annealing under different annealing conditions in the air is shown in Figure 2 and the state of the edges of the same samples is shown in Figure 3 (only the cases where states are different than those on the flat surfaces are shown). Neither the flat surfaces nor the edges show any signs of visible decarburization during annealing at $T_a \leq 700$ °C

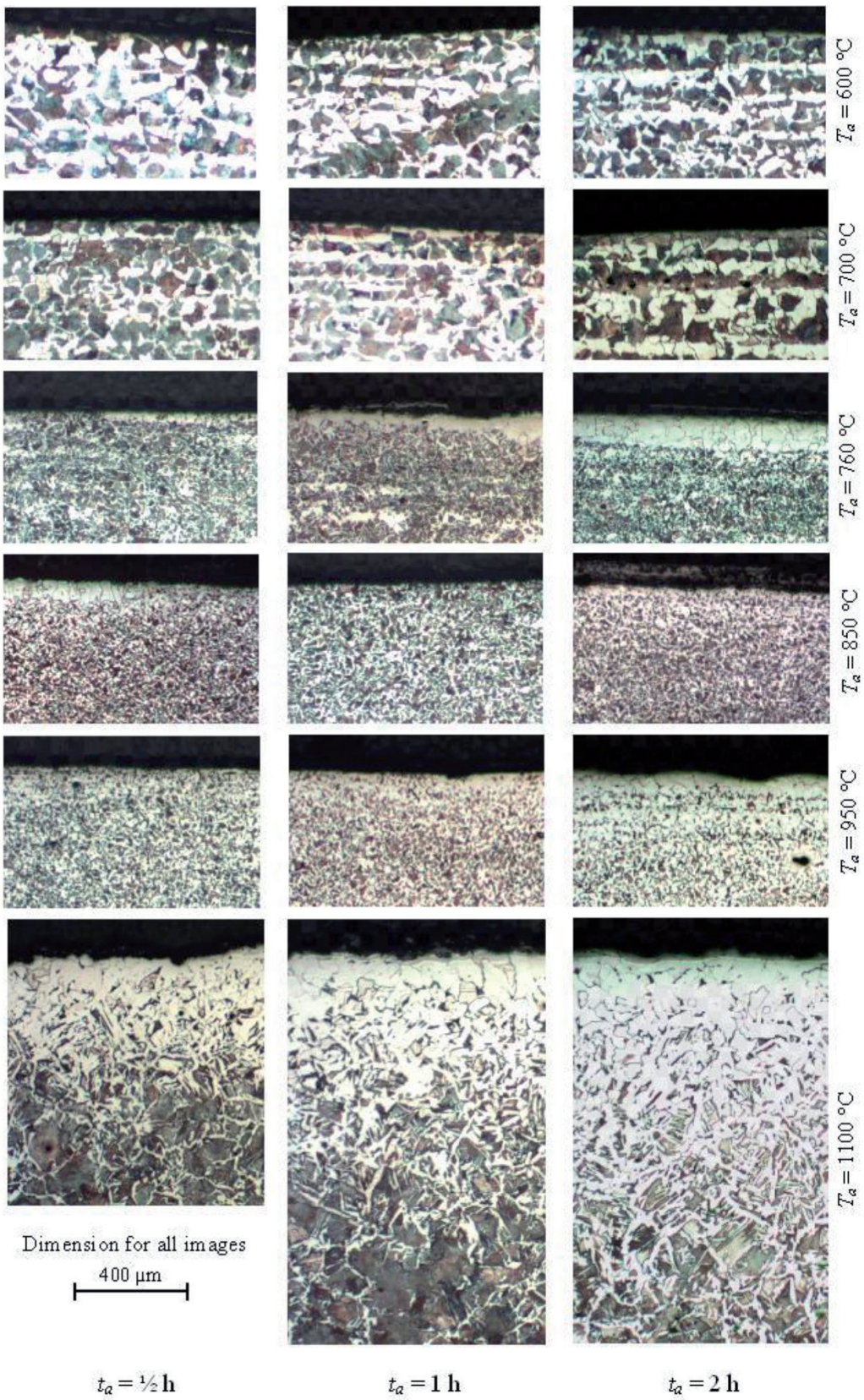

Figure 2: *Microstructural state of the flat surfaces of the steel C45 after annealing in air.*

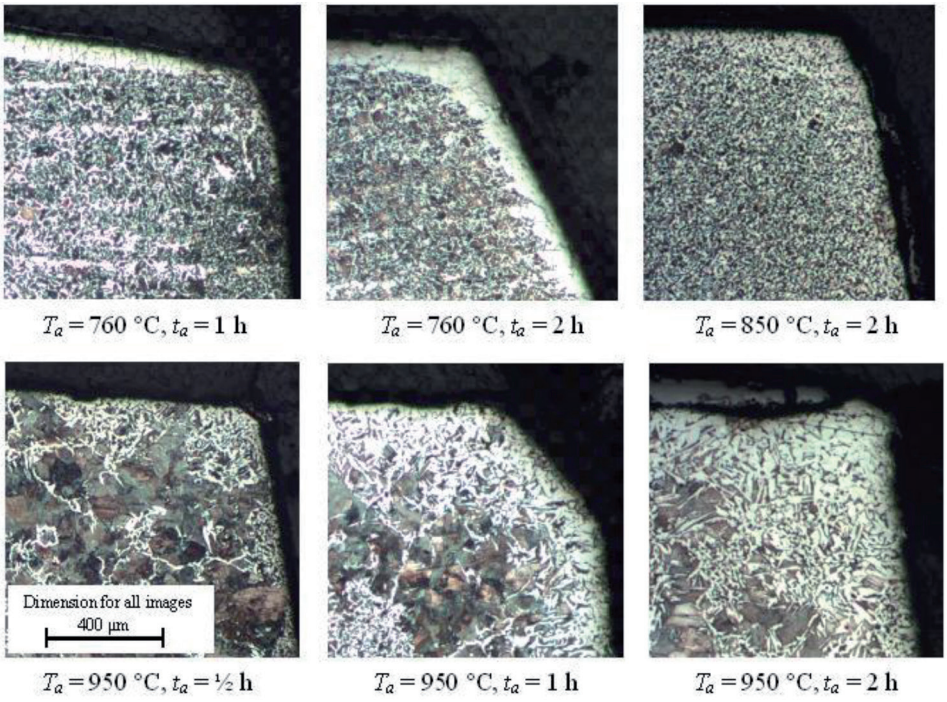

Figure 3: *Microstructural state of the edges of the steel C45 after annealing in air.*

and $t_a \leq 2$ h, which is in agreement with the data of other researchers [4,5]. It appears that the annealing time is too short, as according to some data and for a visible decarburization at $T_a = 700$ °C, the annealing times have to be up to $t_a = 32$ h [5,17]. It seems that under these annealing conditions the speed of decarburization is slower than the speed of oxidation, which is a consequence of the carbon being bound in the Fe_3C. Furthermore, it seems that the scale (thickness calculated at $d_{ox} = 58$ µm after the annealing at $T_a = 700$ °C and $t_a = 2$ h) is still compact enough to make it impermeable to gases, which means that decarburization does not begin.

The microstructure of steel during the annealing at temperatures $T_a = 760$ °C ($A_{C1} < T_a < A_{C3}$) is austenitic–ferritic all the time, which is proven by the larger untransformed ferritic grains in the fine-grained ferritic-perlitic microstructure. Based on Figure 1 the surface becomes purely ferritic after a certain time. This was also proven with our results. After annealing for $t_a = ½$ h the flat surface and the edges did not become decarburized (there is only one local decarburized area on the flat surface, which does not affect the surface properties and could be mistaken for untransformed ferrite). Oxidation of the surface in the first half an hour of annealing is obviously faster than the decarburization, while the scale is thin and compact (calculated thickness of the scale is $d_{ox} = 54$ µm). The decarburized ferritic layer is clearly visible after annealing for $t_a = 1$ h (calculated thickness of scale is $d_{ox} = 76$ µm, so it already cracks and is permeable to gases), but there are also still parts of the surface without visible decarburization. After annealing for $t_a \leq 1$ h the edges did not become decarburized, which means that the edges also experienced only local decarburization. It seems that the factors which control the decarburization process under these conditions are local segregations in the steel and different oxidation speeds in different surface areas (decarburization on the edges should be more visible since the oxidation there is slower [18]; but on the other hand the slower oxidation on the edges means that the scale is still thin enough not to crack, which means it is still impermeable for gases, and therefore the edges were not decarburized). After annealing for $t_a = 2$ h the decarburized layer is continuous, regardless of

surface type, which shows that the oxidation is slower than the decarburization under these conditions. The calculated value of the scale's thickness is d_{ox} = 107 μm, which means that it is permeable to gases. The visible surface ferritic layer of the surface already forming during the annealing in the ferritic–austenitic microstructure as a result of carbon concentrating in the austenite and carbon diffuses towards the surface through the ferritic layer, which consequently caused the simultaneous transformation of austenite into ferrite. This ferrite therefore frontally grows into the austenite (the only part where the austenite can become depleted with carbon is on the inner boundary with the ferritic surface layer; this is because of the carbon diffusion towards the surface through the ferritic layer).

When annealing at T_a = 850 °C ($A_{C3} < T_a < 912$ °C) the steel has the austenite microstructure at the beginning. After some time the surface layer becomes purely ferritic, which is a consequence of the carbon reacting with an oxidative atmosphere (the surface layer goes from the γ area through the α+γ area to the α area) as shown in Figure 1. After annealing for ta = ½ h there is a visible locally limited total and partial decarburization, after t_a = 1 h the decarburization is not visible, while there is only visible partial decarburization of the surfaces and the edges after annealing for t_a = 2 h (it seems that the oxidation is already too fast for a ferritic layer to form). The scale is certainly permeable to gases (the calculated value of the scale after annealing for t_a = ½ h is d_{ox} = 118 μm). It seems that for the shortest times the speed of oxidation is slower than the speed of decarburization, while for the longest times the speed of oxidation of the flat surfaces is in general the same or higher than the speed of decarburization. Non-decarburized areas and locally decarburized areas are a consequence of segregations in the steel and different adherence of the scale on the steel's surface. After cooling, even the edges show the ferritic–pearlitic microstructure consisting of fine grains, which means that under these conditions there was still no overheating. While annealing at temperatures T_a = 950 °C and 1100 °C ($A_{C3} < T_a > 912$ °C) the steel has an austenitic microstructure all the time. Due to decarburization the carbon concentration in the austenite (based on Figure 1) increases from the decarburized surface towards the interior of the sample in accordance with Fick's second law. After cooling the austenite transforms into ferrite and pearlite. At annealing temperatures and times of T_a = 950 °C and t_a = ½ h there is some local decarburization on the flat surfaces. For practical uses this level of decarburization is negligible. This, however, does not mean that there is no decarburization going on. Based on calculations the oxide layer is d_{ox} = 83 μm even after just 3 minutes of annealing, which means it quickly becomes permeable to gases. It seems that the speed of oxidation is the same or faster than the speed of the decarburization. Even when annealing for longer times flat surfaces will show only local decarburization, while the edges are already highly decarburized. It is, however, possible to find areas with the surface ferritic layer.

Another feature seen on the edges is overheating. This is proven by nests of pearlite grains and a Widmanstätten microstructure. It seems that annealing temperatures of T_a = 950 °C are already high enough for some austenite grains in non-alloyed steel to grow. This is also mentioned and shown in [1]. After annealing at T_a = 1100 °C the surface layer becomes highly decarburized, regardless of the annealing time. The same happens with the microstructure, which, regardless of the annealing time, consists of a purely ferritic layer on the surface and a Widmanstätten microstructure below. At this temperature it becomes clear that the diffusion of carbon on the austenite grain boundaries is of much higher magnitudes (because of the decarburized austenitic grain boundaries there will be polygonal ferrite present at these boundaries after cooling; Widmanstätten ferrite grows from this polygonal ferrite into the interior of the pearlitic grains) and that the decarburization speed is much higher than the rate of oxidation.

The edges are therefore more prone to decarburization than the flat surfaces, while they are also a critical area for overheating. In steel C45 at temperatures $T_a \geq 950$ °C this is responsible for a locally or globally present coarse-grain austenitic microstructure, which is shown by nests of pearlitic grains (Figure 3). This is certainly a consequence of locally converg-

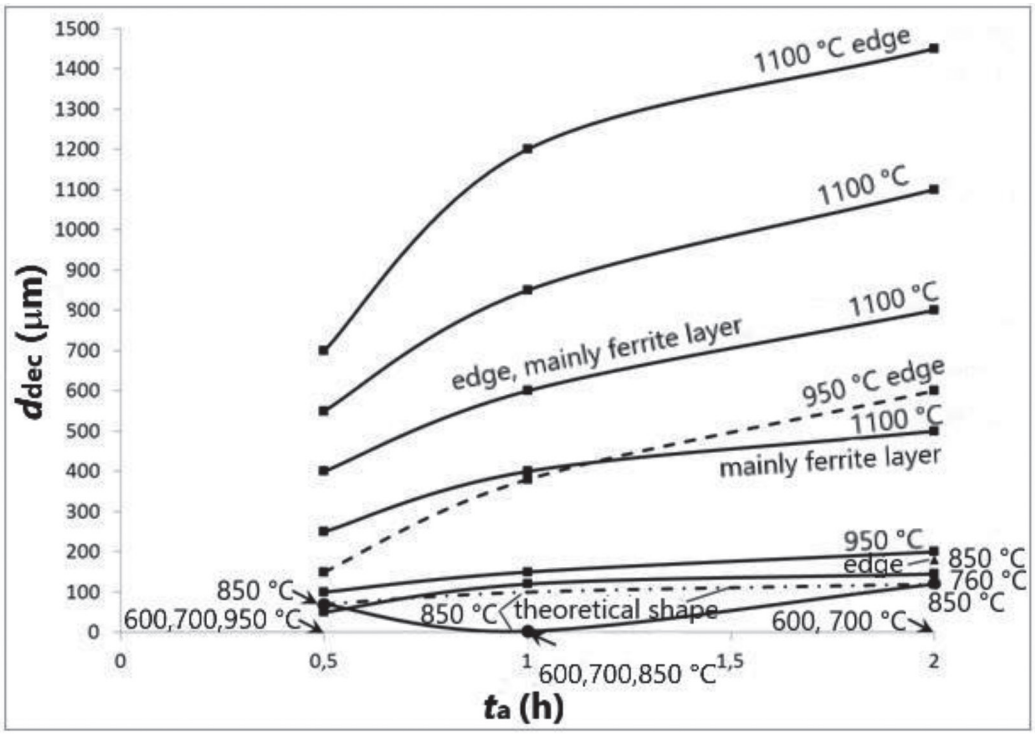

Figure 4: *Maximum depth of visible decarburized layer d_{dec} of steel C45 after annealing in air.*

ing surfaces (edges are subjected to annealing temperatures for longer times than the flat surfaces) and different conditions for oxidation (it is usually of lower intensity than on the flat surfaces [18]). The conclusion is that different geometrical features affect the process of decarburization under the same annealing conditions.

The measured maximum depths of the decarburization are shown graphically in Figure 4. Our results are in accordance with the findings [8,16] that decarburization follows a parabolic law like the oxidation. For the decarburization at T_a = 850 °C two curves are plotted. The dashed line shows the generally well-known parabolic shape of the decarburization, while the full line represents the real state of the decarburization obtained from the measurements. The results show that at this temperature the shorter time of annealing in the air is more critical than a longer time (on the surface a fully decarburized ferritic layer forms after annealing for t_a = ½ h, while the ferritic surface layer is not visible when annealed for longer times).

There is a time interval of annealing in the air when visible decarburization does not exist. This is undoubtedly related to the oxidation rate of the surface, which is also confirmed by the results in [19,20]. In this case the decarburization of the steel was studied in an atmosphere consisting of N_2 and 4 vol.% natural gas in which a different amount of air was added. Under the following annealing conditions (T_a = 850 °C in t_a = 2 h and the content of air is less than 8 vol. %) the decarburization increases. However, when more than 8 vol. % of air was added a significant difference in the decarburization depths was found (the curve in the Figure 4 [20] is dashed and describes a theoretical process of decarburization), which is explained by surface oxidation. The oxidation and various impact factors (the chemical composition of the steel, the volume of the furnace chamber, different types of chamber furnace, i.e., with or without a fan, the ratio between the volume of the chamber and the sample, the air flux in the furnace, the air's humidity) are certainly a reason for the huge deviations in the decarburization depth measurements found in the literature. The effect of the humidity of the non-air atmospheres is known (if the humidity is higher, then the dew point is also higher,

the carbon potential of the atmosphere is lower and the decarburization is stronger [20]). However, according to known facts (due to water vapour in air the adherence of the scale to the steel surface is better and thus, the oxidation rate is higher [14]; the oxidation rate of steel is two to three times higher in air supersaturated with moisture [21]) the visual decarburization in the wet air is supposed to be decreased in comparison to the dry air (the effect of the humidity might be important only in a certain temperature range).

Conclusions

In this research the decarburization of normalized, non-alloyed, hypo-eutectoid carbon steel C45 annealed in an air atmosphere was investigated. Based on the results it can be concluded:

- The rates of decarburization and oxidation for the surface increase with higher temperatures and longer annealing times. Compared to the flat surfaces, the edges had a higher degree of decarburization, in general. There was no visible decarburization of the surface of the C45 steel under some annealing conditions. These are: $T_a \leq 700$ °C for $t_a \leq 2$ h, $T_a = 760$ °C for $t_a = 1/2$ h and $T_a = 850$ °C for $t_a = 1$ h. The rate of oxidation of the surface under these annealing conditions is higher than the rate of its decarburization. This means that stress relieving, normalizing and annealing for quenching can be carried out in air.
- Locally limited decarburization of the surface was discovered when annealing at $T_a = 760$ °C for $½ \text{ h} < t_a < 1$ h, $T_a = 850$ °C for $t_a = ½$ h and 2 h and $T_a \leq 950$ °C for $½ \text{ h} < t_a \leq 2$ h. The speeds of oxidation and decarburization are approximately the same under these conditions, which means that one of the possible reason for locally decarburization is a consequence of segregations. This increases the activity of carbon in those areas (because silicon does not segregate a lot, the only other option in C45 steel is that these segregations have a lower manganese concentration than the rest of the steel). The occurrence of locally decarburized areas is time dependent until the global decarburization happened (in our case this happened at $T_a = 760$ °C, $t_a = 2$ h and $T_a = 1100$ °C). A second, probably more possible reason for local decarburization could be a different adhesion of the scale to different parts of the steel's surface and local cracking of the scale. Under these annealing conditions it is necessary to introduce measures to prevent the oxidation and decarburization (for example, annealing in a protective atmosphere).
- Highest rates of decarburization occur during high-temperature annealing where the coarse austenite crystal grains also occur due to overheating. Those grown austenite grains lead to a coarse Widmanstätten ferritic–pearlitic microstructure at room temperature. When annealed at $T_a = 950$ °C for $½ \leq t_a \leq 2$ h, the areas that were most prone to overheating and decarburization were the edges. Other surfaces became prone to those when being annealed at $T_a = 1100$ °C for $t_a \geq ½$ h. Under these annealing conditions it is necessary to introduce measures for the prevention of oxidation and decarburization.

References

[1] Schumann, H. (1983): *Metallografie*, *12. Auflage*. Leibzig: WEB Deutscher Verlag für Grundstoffindustrie, 608 p.

[2] Kveder, A. (1972): *Metalurški priročnik (Handbook of Metallurgy)*, Ljubljana: Tehniška založba Slovenije, 1471 p.

[3] Mardon, C. (1998): *The austenitization and decarburization of high silicon spring steel*. PhD Thesis, Christchurch: University of Canterbury; 103 p.

[4] Zhang, C.L., Zhou, L.I., Liu, Y.Z. (2013): Surface decarburization characteristics and relation decarburized types and heating temperature of spring steel 60Si2MnA. *International Journal of Minerals, Metallurgy, and Materials*, 20(8), pp. 720–724.

[5] Liu, Y., Zhang, W., Tong, Q., Wang, L. (2014): Effects of Temperature and Oxygen Concentration on the Characteristics of Decarburization of 55SiCr Spring Steel. *ISIJ International*, 54(8), pp. 1920–1926.

[6] Zorc, M. (2016): *Decarburization of non-alloy medium carbon steel during annealing in an air atmosphere* (in Slovenian), Diploma Thesis, Ljubljana: University of Ljubljana, Faculty of Natural sciences and Engineering - Department of Materials and Metallurgy; 41 p.

[7] Mayott, S.W. (2010): Analysis of the Effect of Reduced Oxygen Atmospheres on the Decarburization Depth of 300M Alloy Steel, Master of Science Thesis, New York, Rensselaer Polytechnic Institute, Department of Materials Science and Engineering.

[8] Naumann, F.K. (1976): *Das Buch der Schadensfälle*. Stuttgart, Germany: Dr. Riederer-Verlag GmbH, 481 p.

[9] Vander Voort, G.F. (2015): Understanding and Measuring Decarburization. *Advanced materials & Processes*, 173(2), pp. 22–27.

[10] Jaason, K., Peetsalu, P., Saarna, M., Kulu, P., Beilmann, J. (2016): Decarburization Effect on Hardened Strip Fastening Components. *Materials Science*, 22(1), pp.148–152.

[11] Vodopivec, F. (2002). *Kovine in zlitine* (Metals and Alloys), Ljubljana: Institute of Metals and Technology, 474 p.

[12] Zorc, B., Nagode, A., Kosec, B., Kosec, L. (2013): Elevator chain wheel shaft break analysis. *Case Studies in Engineering Failure Analysis,* 1(2), pp. 115–119.

[13] Atlas zur Wärmebehandlung der Stähle auf CD-ROM (2009); Düsseldorf: Verlag Stahleisen GmbH.

[14] Chen, R.Y., Yuen, W.Y.D. (2003): Review of the High-Temperature Oxidation of Iron and Carbon Steels in Air or Oxygen. *Oxidation of Metals*, 59(5/6), pp. 433–468.

[15] De Cooman, B.C., Speer, J.G. (2011): *Fundamentals of Steel Product Physical Metallurgy*, Englewood: AIST, 642 p.

[16] Grzesik, Z. (2003): Thermodynamics of Gaseous Corrosion. In ASM Handbook, Vol. 13A - Corrosion: Fundamentals, Testing, and Protection, Cramer, S.D., Covino Jr., B.S. (Eds.), Ohio: ASM International, Materials Park, pp. 90–96.

[17] Billings, G.A. (1966): Oxidation and Decarburization Kinetics of Iron-Carbon Alloys in Carbon Dioxide-Carbon Monoxide Atmosphere, Master of Science Thesis, Hamilton, Ontario: McMaster University; 120 p.

[18] Baud, J., Ferrier, A., Manenc, J., Bénard, J. (1975): The oxidation and decarburizing of Fe-C alloys in air and the influence of relative humidity. *Oxidation of Metals*, 9(1), pp. 69–97.

[19] Sebenji, F., Hakl, L., (1980). *Corrosion of metals in theory and practice* (in Serbian), Belgrade: Tehnička knjiga, 226 p.

[20] Stratton, P.F. (1984): Living with Furnace Atmosphere Contamination. Metal Science and Heat Treatment, 2, pp. 41–48.

[21] Parrish, G. (1999): *Carburizing-Microstructures and properties*. Ohio: ASM International: Materials Park, 247 p.

[22] Mladenović, S., Petrović, M., Rikovski, G. (1975). *Handbook of chemical technology, Corrosion and protection of materials* (in Serbian), Belgrade: IRO "RAD", 484 p.

Original scientific paper

Received: May 01, 2018
Accepted: Jun 08, 2018
DOI 10.2478/rmzmag-2018-0015

Wire arc additive manufacturing of mild steel

3D obločno oblikovno navarjanje z žico iz konstrukcijskega jekla

Damjan Klobčar[1,*], Maja Lindič[1], Matija Bušić[2]

[1] Faculty of Mechanical Engineering, University of Ljubljana, Aškerčeva 6, 1000 Ljubljana, Slovenia

[2] Faculty of Mechanical Engineering and Naval Architecture, University of Zagreb, Ivana Lučića 5, 1000 Zagreb, Croatia

* damjan.klobcar@fs.uni-lj.si

Abstract

This paper presents an overview of additive manufacturing technologies for production of metal parts. A special attention is set to wire arc additive manufacturing (WAAM) technologies, which include MIG/MAG welding, TIG welding and plasma welding. Their advantages compared to laser or electron beam technologies are lower investment and operational costs. However, these processes have lower dimensional accuracy of produced structures. Owing to special features and higher productivity, the WAAM technologies are more suitable for production of bigger parts. WAAM technology has been used together with welding robot and a cold metal transfer (CMT) power source. Thin walls have been produced using G3Si1 welding wire. The microstructure and hardness of produced structures were analysed and measured. A research was done to determine the optimal welding parameters for production of thin walls with smooth surface. A SprutCAM software was used to make a code for 3D printing of sample part.

Key words: robotic MIG/MAG weld surfacing, hardness, wire arc additive manufacturing (WAAM), SprutCAM.

Povzetek

Ta članek prikazuje pregled dodajalnih tehnologij na področju izdelave kovinskih izdelkov. Podrobneje je predstavljen postopek 3D obločnega oblikovnega navarjanja z žico – WAAM (ang. Wire and arc additive manufacturing), ki temelji na postopkih navarjanja MIG/MAG, TIG ali plazemskega navarjanja. Njegova prednost v primerjavi z navarjanjem z žarki, kot sta laser in elektronski snop, so nizki investicijski stroški in operativni stroški. Omejitev teh tehnologij je njihova nižja dimenzijska natančnost. Zaradi posebnosti postopkov navarjanja in velike produktivnosti je tehnologija izdelave WAAM bolj primerna za izdelavo izdelkov večjih dimenzij. Pri eksperimentalnem delu smo uporabili vir varilnega toka CMT in varilnega robota. Tanke stene smo izdelali z varilno žico G3Si1. Izmerili in analizirali smo mikrostrukture in trdoto navarjenih sten. Z raziskavo smo določili optimalne parametre za izdelavo tankih sten z nizko valovitostjo. Za generiranje kode za 3D navarjanje reprezentativnega izdelka enostavne geometrije smo uporabili programsko okolje SprutCAM.

Ključne besede: robotsko navarjanje MIG/MAG, trdota, oblikovno obločno navarjanje z žico (WAAM), SprutCAM.

Introduction

American Society for Testing and Materials [ASTM] defined additive manufacturing as a process of joining materials layer by layer to make objects from 3D data. There are many differences between additive manufacturing compared to subtractive manufacturing. Many terms are used for this technology: additive manufacturing, additive process, additive technology, 3D printing, rapid prototyping and rapid tooling [1].

The development of additive manufacturing of technologies of metal and polymer parts does not progress evenly. Existing market solutions enable manufacturing of complex parts in tight tolerances. The cost of parts depends on precision and quality of manufacturing. For example, development of polymers' rapid prototype is already at a high level. One can buy low-cost 3D printers, which are available for home use. The advantages of these systems is user friendliness and inexpensiveness, but they have limitations in the manufacturing process [1, 2].

There are many different technologies that are developed in additive manufacturing of metal parts. "Electric arc using heat as power source for 3D parts by welding in layers" was patented in 1926 by Baker. Pressure vessels were made with SMAW and TIG welding by using different filler wires for building walls by Ujiie (Mitsubishi) in 1971. Shape welding was used for producing large, 79 tons heavy, high-quality nuclear structural parts made from 20MnMoNi 5 with build rate of 80 kg/h by Kussimaul in 1983. In 1993, Prinz and Weiss patented the process, which was the combination of welding and CNC milling and named it "Shaped Deposition Manufacturing – SDM" [3, 4] for the Rolls Company for castings. Through the years, they developed a variety of processes and materials, the process itself is still used in manufacturing. In 2006, companies expressed the need for rapid prototyping from titanium. Engineers tried to find the replacement for non-sustainable traditional subtractive manufacturing. The prediction for the next 20 years is that aircraft industry will need over 18 million tons of titanium wherein the buy-to-fly ratio is 5. This means that 72 million tons of titanium will be a waste material [5–8].

Additive manufacturing of metal parts can be divided based on technologies using beams and arcs (Figure 1). Laser beam or electron beam could be used for printing of metal parts. Filler material in this case is powder or wire. In laser systems, the feed powder can be added with gas (blowing), a process called laser cladding. In selective laser sintering (SLS) or electron-beam melting (EBM), powder in containers can be used. In laser systems, wire is added from side or perpendicular to the welding spot. In case of welding with electron beam, we use the Sciaky system. MIG, TIG and plasma are most common in arc welding. In all variations, the feeding material in the form of wire is being used. The common expression for all these technologies is wire arc additive manufacturing – WAAM [5]. The most common system used for WAAM is industrial robot, where welding torch is installed. The price of such a system is up to 300 k€ for building less complex parts. For production of high-quality parts suitable for aerospace technology, systems consisting of high-cost CNC and robot are required. Their price are in the range of 0.2–2 M€ [2]. Structure stiffness, dynamic accuracy and vibration damping of CNC machines are higher, so they are more appropriate for manufacturing by WAAM [3].

There are many disadvantages of using powder instead of wire: High costs, variable powder quality, complexity of feed unless the side feed system is being used, low efficiency (40–60%), careful handling because of safety aspects and head rotation problems if feed is added from side. When adding the wire filler material, the price of materials is medium–high and the quality of the material is high (Ti, Fe, Ni), but this could be different when using aluminium alloys. The efficiency of feed material is close to 100%, the feeding system is already developed, the recycling of materials is not necessary and head rotation problems turn up only when using plasma and TIG welding. Feed material outside the required position is possible [5].

The purpose of this research was to determine optimal technological welding parameters for WAAM of thin welds that could result with stable depositions in heights at different welding positions. Standard MAG (with shielding gas CO_2), impulse MIG (with shielding gas Ar) and cold metal transfer (CMT) process at pre-

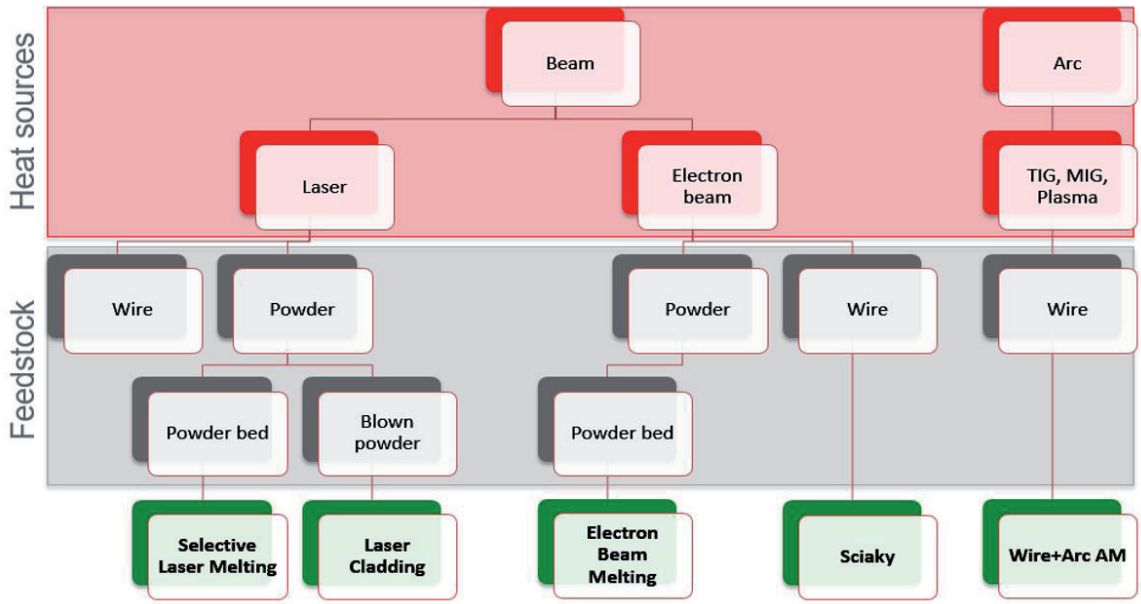

Figure 1: *The partition of additive manufacturing of metal parts [5].*

liminary welding have been analysed. Different welding currents (40 A, 90 A, 140 A) and welding speeds (3 mm/s, 7.5 mm/s, 12 mm/s) were investigated. Based on preliminary tests, to achieve optimal welding conditions, the CMT process has been selected for future optimisation. During welding in different positions, PA, PC and PG temperatures of layers have been measured. Demonstration products were made with optimal welding parameters using the SprutCAM software [9].

Comparing energy inputs by laser or arc technologies show high investment and operational costs when using laser and low cost when using plasma or MIG. Total efficiency and joining efficiency are approximately 10% using laser and 80% using arc. There is also a high safety risk when using laser technologies, but they have medium to high build rate compared to that of arc technologies. Minimum thickness of 0.2 mm layer can be achieved with laser technologies compared to 1 mm with arc technologies [5].

Comparison between layer heights, build rate and horizontal resolution suggests that powder bed technologies have the lowest build rate and a high resolution, while technologies based on blowing powder have a high build rate and a low resolution. WAAM technology has a higher build rate and lowest resolution compared to powder technologies. When melting efficiency is maximal, the build rate depends on squared layer height for single axially symmetric source. Resolution has many influencing factors, and it depends on layer height to width ratio, usually is the best in 1.5 layer to height ratio [5], because low-resolution parts commonly need post-machining treatment process to fit the geometrical tolerances. Treatment can be done intermediately or post process, depending on requirement result. Intermediate machining done between deposited layers allows adjustment of layer thickness and machining of internal surfaces in case of shell parts in comparison to post machining, which does not support such machining but is less time-consuming.

Experiment

MAG process has been used on S355 structural steel base plate in dimensions 100 × 22 × 8 mm. G3Si1 welding wire in 1.2 mm diameter has been used with shielding gas CORGON 18 (82% Ar + 18% CO_2) with a flow rate of 10 l/min. Fronius TransPuls Synergic 3200 CMT power source and welding robot ABB IRB 140 have been used as a WAAM equipment. From the produced structures, specimens have been sectioned for analysis of microstructure, Vickers

hardness and tensile strength at different orientations relative to the direction of welding wire feed. Zwick/Z250 machine has been used for tensile tests and 2% nital etch (a solution of nitric acid and alcohol) for preparation of specimens for analysis of structure using optical microscope Mitutoyo TM.

Results and discussion

Welding parameters that allow stable welding for thin walls have been determined. One layer deposited on base plate of 8 mm thickness built with welding current 40 A is shown in Figure 2. In the case of standard control of wire feed, the weld was acceptable only at the lowest speed of welding and highest energy input (137.3 kJ/m). Energy input at a higher welding speed was too low to build an acceptable weld. In the case of pulse control of wire feed, an acceptable weld has been made with a welding speed of 7.5 mm/s and energy input of 94 kJ/m. All welds were of sufficient quality when using CMT at all welding speeds and also at a higher energy input (34.3 kJ/m). Welds were wider than in other cases.

Welds made by the CMT process at a welding current of 40 A are shown in Figure 3. In the picture above were welding took place from right to left, on the median and lower from left to right. Welds were acceptable only when welding was carried out at a speed of 3 mm/s. There were problems with the arc ignition at the start and melting of material at the end. Because of the unstable process, cavity occurred at start of the welds. If energy input is decreased, stability of welding process is reduced when welding walls. The process of welding cannot be performed at the deposition of only a few layers. The welding of the wall after process optimisation, at a welding current of 90 A and a welding speed of 3 mm/s from right to left, is shown in Figure 4a. It can be noticed that the thickness of wall increased and sloping appeared. This is because of wall overheating at the end of welding and spilling of deposited material. Sloping can be partially improved by changing welding direction by the welding of each layer, which is shown in Figure 4b.

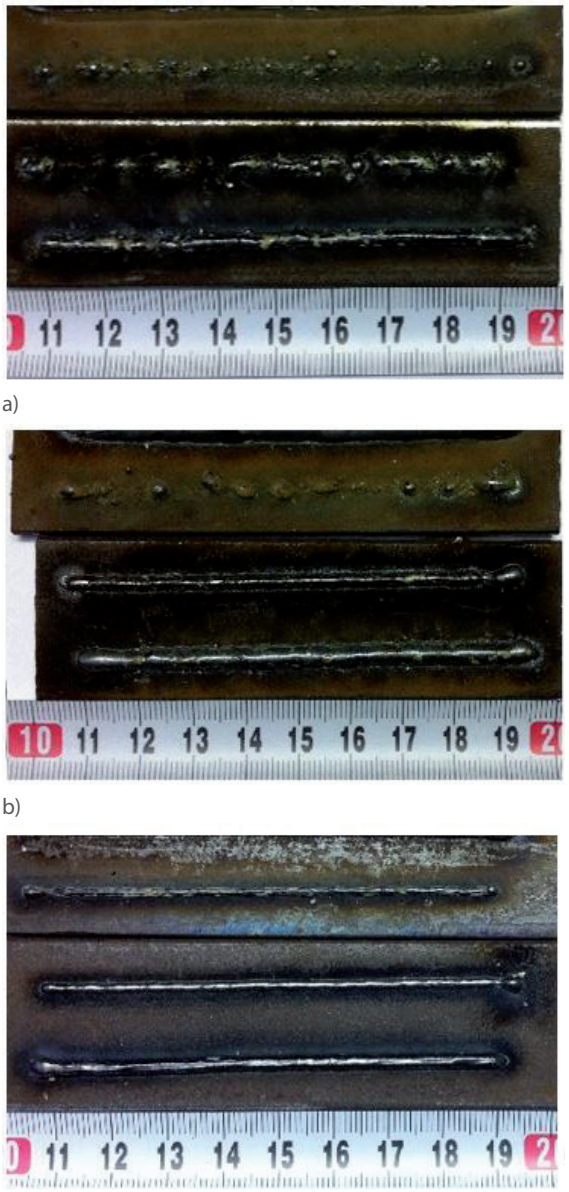

Figure 2: *Welding at 40 A a) standard, b) pulse and c) CMT (different welding speeds from bottom to top: 3, 7.5 and 12 mm/s).*

Based on parametric analysis and geometry measurement, weld width and height decreased if welding speed was increased (shown in Figure 5). If welding current increased, consequently welding wire feed speed, energy input, welding height and welding width increased. In case of welding many layers with a high weld inter-pass temperature (200°C), weld width increased and weld height decreased at a constant volume. One of the impacts on weld height and width besides welding parameters is also inter-weld temperature.

Figure 3: *Welding by CMT process at welding current 40 A (different welding speed from top to bottom: 3, 7.5, 12 mm/s).*

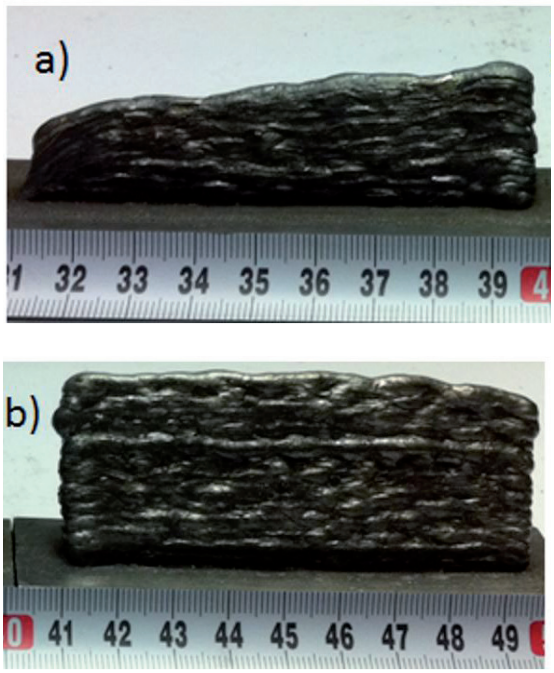

Figure 4: *Welding influence at I = 90 A, v = 7.5 mm/s a) at left and b) alternate on both sides.*

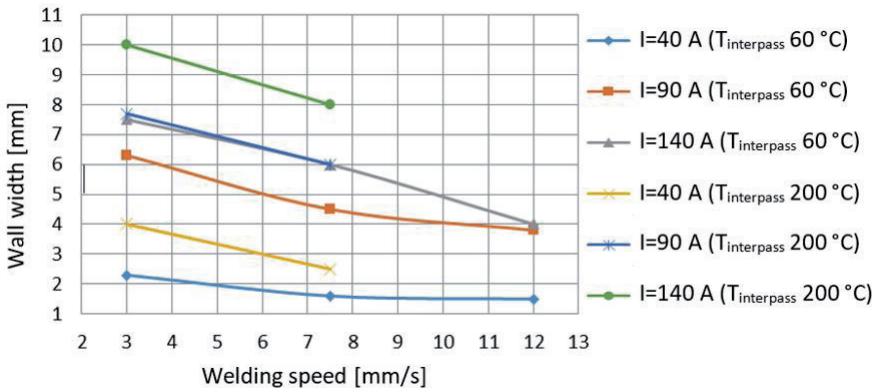

a)

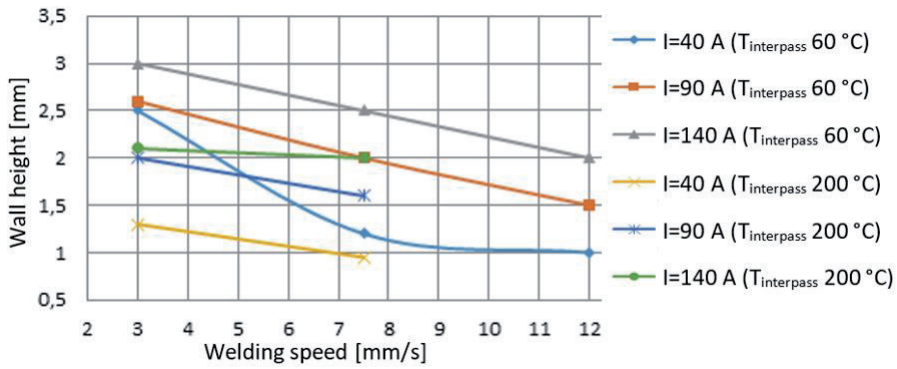

b)

Figure 5: *Influence of welding parameters for CMT process on: a) bead width and b) weld height.*

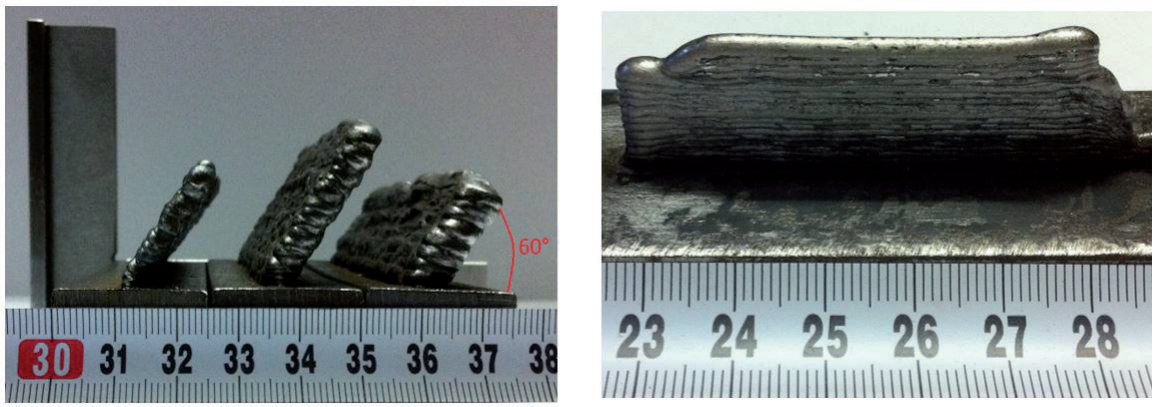

Figure 6: *Welding in a) PA position at parameters: I = 40 A, v = 5mm/s; I = 90 A, v = 7.5 mm/s; I = 140 A, v = 7.5 mm/s and angle of torch 60° and b) PG position at parameters: I = 40 A, v = 5mm/s.*

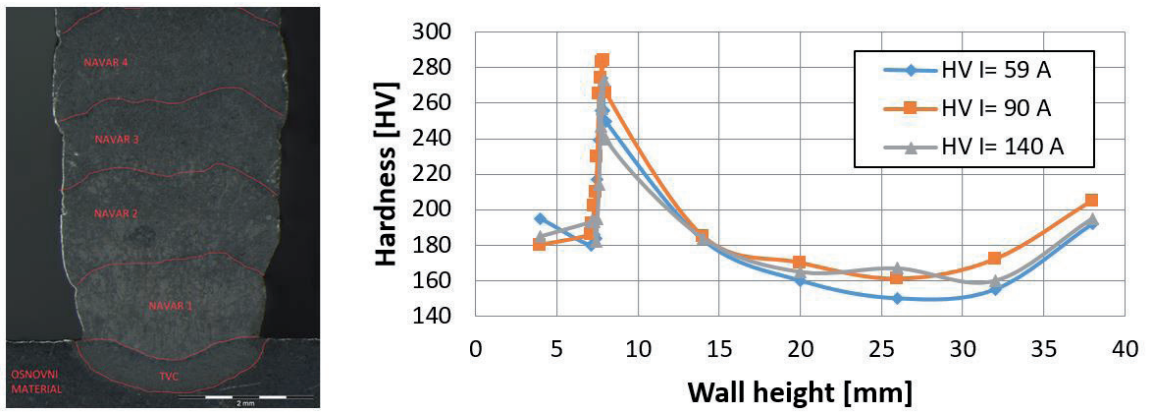

Figure 7:

Figure 8:

Welding in difficult positions and different angles of torch was also performed. The inter-weld temperature had, besides energy input, a great influence in all cases. Welds made in the PA position with different energy inputs are shown in Figure 6a. Torch angle was 60°and was equal to the wall angle, which was built. Welding made in the PG position (welding from up to bottom)

by increasing weld inter-pass temperature developed a droplet of material at the end of weld because of the influence of gravity (shown in Figure 6b.) The height of weld increased too.
Figure 7a presents macro of weld made at a welding current of 59 A and a welding speed of 5 mm/s. The first weld is narrower and higher because of increased heat transfer into colder base plate. Weld thickness in layers above was increased because of lower heat transfer and higher inter-weld temperature. Hardness in layers is shown in Figure 7b. Hardness was measured in different spots in HAZ, where it was increased up to 280 HV value. The hardness value of the base plate was measured at 190 HV. Hardness at layers above was measured in the middle of each layer. Failure of welds in upper layers has been detected. Hardness decreases from value 200 HV to 160 HV. Welded layer was softer compared to the base plate for approximately 20 HV.
The 3D model of demonstration part built with WAAM technology is shown in Figure 8. The process was continuous without controlling inter-weld temperature. Inter-weld temperature was high, which can be seen on the middle picture where the part being built was still glowing. The shape of the 3D model corresponds to the shape of the part made with the WAAM technology. Because of higher inter-weld temperature, there is a rough surface and material spillage over the part built. Smoother surface caused with a few second of pause, which provided lower inter-weld temperature.

Conclusion

A parametric analysis of weld surfacing (WAAM) of thin walls was done using MIG/MAG technology and welding filler wire G3Si of diameter 1.2 mm. The following was established:

— A combination of pulse and CMT welding presented the optimal process control program. Optimal welding parameters for weld surfacing of thin layered walls were obtained at a welding current of 59 A, welding voltage of 8.8 V and welding speed of 5 mm/s, where the linear heat input was 103.8 kJ/m.
— Welding parameters together with inter-pass weld temperature should be considered to provide stable surfacing process. Inter-pass weld temperature should not exceed 100°C, to avoid spilling of the molten metal.
— Energy input should be between 100 and 300 kJ/m. If linear energy input is too low, wavy surface may appear, and if it is too high, there can be a spilling of material with changed height to width ratio.
— Hardness of material is very constant; it only changes in HAZ.
— Welding in different positions can be done, but the most convenient is to do it in the PA position. In other positions, the influence of gravity, surface tension and inter-pass weld temperature should be considered with keeping energy input minimised.

Acknowledgements

The authors wish to thank Luka Bricelj and Boris Bell for conducting experimental work, Nikolay Konov for the help with SprutCAM software, company SIJ Elektrode Jesenice for supporting them with filler metals and company GTG plin d.o.o. for support with their shielding gasses. The authors acknowledge the financial support from the Slovenian Research Agency (research core funding no. P2-0270 and Project Nos. L2-8181 and L2-8183). The article is in part the result of work in the implementation of the SPS Operation entitled MAterials and Technologies for New Applications – MARTINA. The investment is co-financed by the Republic of Slovenia and the European Union from the European Regional Development Fund.

References

[1] Frazier, W. E. (2014): Metal additive manufacturing: A review. *Journal of Materials Engineering and Performance,* 23(6), pp. 1917–1928.
[2] Wong, K.V., Hernandez, A. (2012): A review of additive manufacturing. *ISRN Mechanical Engineering,* 2012, pp. 1–10.
[3] Merz, R. (1994): *Shape deposition manufacturing* (Doctoral dissertation), Retrieved from https://www.researchgate.net/publication/30873042_Shape_deposition_manufacturing, pp. 169.

[4] Weiss, L.E., Merz, R., Prinz, F.B., Neplotnik, G., Padmanabhan, P., Schultz, L., Ramaswami, K. (1997): Shape deposition manufacturing of heterogeneous structures. *Journal of Manufacturing Systems*, 16(4), pp. 239–248.

[5] Williams, S.W., Martina, F., Addison, A.C., Ding, J., Pardal, G., Colegrove, P. (2016): Wire+ arc additive manufacturing. *Materials Science and Technology,* 32, pp. 641–647.

[6] Martina, F., Roy, M.J., Colegrove, P.A., Williams, S.W. (2014): Residual stress reduction in high pressure interpass rolled wire+ arc additive manufacturing Ti-6Al-4V components. *Proc. 25th Int. Solid Freeform Fabrication Symp*, pp. 89–94.

[7] Colegrove, P.A. et al., (2014): High pressure interpass rolling of wire+ arc additively manufactured titanium components. *Advanced Materials Research*, 996, pp. 694–700.

[8] Nilsiam Y., Haselhuhn, A., Wijnen, B., Sanders, P., Pearce, J.M. (2015): Integrated Voltage—Current Monitoring and Control of Gas Metal Arc Weld Magnetic Ball-Jointed Open Source 3-D Printer. *Machines,* 3(4), pp. 339–351.

[9] SprutCam software [cited 17/8/2018], Available on: <http://*www.sprutcam.com*>.

Original scientific paper

Received: Aug 21, 2018
Accepted: Oct 25, 2018
DOI 10.2478/rmzmag-2018-0022

The Universal Kriging Mapping of the Neogene EL-markers Rs5 and Δ, Northern Croatia

Kartiranje z univerzalnim krigiranjem neogenskih EL-markerjev Rs5 in Δ v severni Hrvaški

Ivana Mesić Kiš[1], Tomislav Malvić[2]

[1] ES kralja Tomislava Našice, Ulica Matice hrvatske 1, 31 500 Našice, Croatia

[2] University of Zagreb, Faculty of Mining, Geology and Petroleum Engineering, Pierottijeva 16, 10 000 Zagreb, Croatia;

* ivy.mesic@gmail.com

Abstract

The area of the Bjelovar Subdepression in Northern Croatia, which represents the southwestern part of Drava's depression, has been analysed. More than 700 depth data were collected in a regular grid covering the existing structural maps of e-log markers Rs5, Z' and Δ, with cells 2 x 2 km in size. For zonal assessment, Thiessen polygon method was used as introductory analysis preceding Kriging interpolation on regional scale. The emphasis was on OK and UK interpolation, their comparison and selection of most appropriate method for mapping. Crossvalidation results proved UK technique to be the most appropriate in mapping of e-log markers Rs5 and Δ, thus acquiring the most accurate maps so far of the analysed Neogene area.

Key words: e-log markers, advanced mapping method, Universal Kriging, Bjelovar Subdepression, Croatia

Povzetek

Analizirali smo območje bjelovarske poddepresije v severni Hrvaški, ki predstavlja jugozahodni del dravske depresije. Zbrali smo nad 700 globinskih podatkov v pravilni meži, ki pokriva obstoječe strukturne karte e-log markerjev Rs5, Z' in Δ s celicami velikosti 2 x 2 km. Za ugotovitev zonalnosti smo uporabili Thiessnovo poligonsko metodo kot uvodno analizo pred krigirno interpolacijo v regionalnem merilu. Poudarek je bil na OK in UK interpolacijah, njuni primerjavi in izbiri najprimernejše metode kartiranja. Navzkrižna preverba rezultatov je potrdila, da je UK tehnika najprimernejša za e-log markerje Rs5 in Δ, kar je omogočilo dobiti najnatančnejše karte analiziranega neogenskega območja do zdaj.

Ključne besede: e-log markerji, sodobna metoda kartiranja, univerzalno krigiranje, bjelovarska poddepresija, Hrvaška

Introduction

First geological explorations of the Bjelovar Subdepression began in the mid-19th century when first sketches and geological maps were made in this area (e.g. [1]). In the 20th century and in recent years the research was mostly directed towards detecting hydrocarbon reservoirs (e.g., [2–4]). E-log markers were used for the interpretation of the geological evolution. They represent layers between two sedimentary or igneous-metamorphic units in the overlaying cover and basement. Over the last 15 years in the area of Bjelovar subdepression, depth maps were made on surfaces of all e-log markers (Rs7, Rs5, Z', Δ and D') and one e-log border (Pt/Tg) that divides the Neogene-Quaternary sediments and older rocks in their basement (e.g. [5]). Maps were interpolated by hand [3,6], while some e-log markers (Rs7 and Rs5) and e-log border (Pt/Tg) were also interpolated using Ordinary Kriging (abbr. OK) technique [7]. This technique was confirmed by numerous Croatian authors as the best method for displaying the spatial distribution of clastic reservoir variables (e.g. [8–11]).

The Universal Kriging technique (abbr. UK), also known as a Kriging with a trend, is slowly finding its place in Croatian geology. It was used for mapping of e-log marker Z' in Šandrovac Field, Croatian biggest and prominent oil and gas field [12], when compared to the OK, gave much better results (RMSE (OK) = 171, RMSE (UK) = 59) due to expressed linear spatial trend. The aim of this paper is to show and explain why the UK technique gives better results for two e-log markers, Rs5 (Lower/Upper Pannonian border) and Δ (the upper part of Upper Pontian) and provides most accurate depth maps so far for analysed Neogene area. In addition, e-log marker Z' had been interpolated (Upper Pannonian/Lower Pontian border) using both OK and UK for better insight of OK and UK differences.

The mapped area of Bjelovar Subdepression is located in the northern part of Croatia, i.e. it is the south-western part of Drava Depression, approximately between 45°20' and 46°5' N, 16°20' and 17°25' E (Figure 1).

Materials and methods for data selection and interpolation

Mapping of the entire Subdepression was done using the square grid cells (2 x 2 km in size) that were laid over the hand interpolated maps (e.g. [7]) of e-log markers Rs5, Z' and Δ (Figure 2) made by [6]. Thiessen polygon method was used for zonal estimation and also as an apparent indicator of regular grid used in

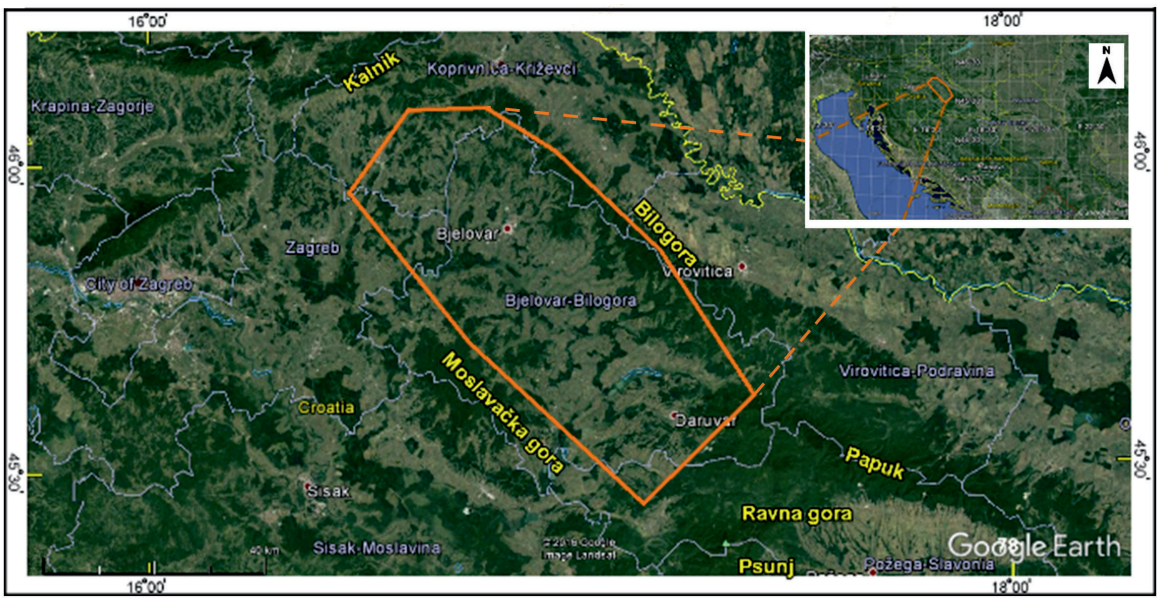

Figure 1: *Geographical location of Bjelovar Subdepression (SW part of Drava Depression, Northern Croatia).*

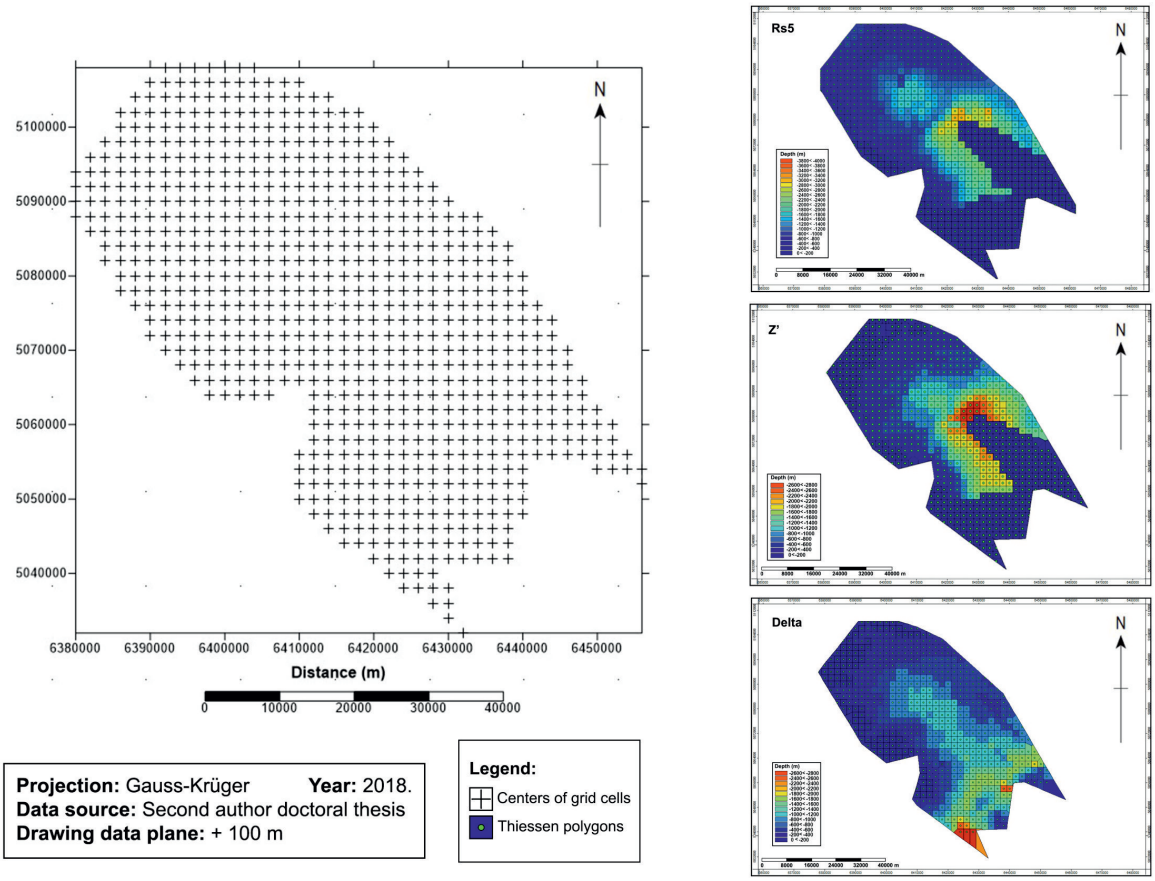

Figure 2: *Regular grid and centers of grid cells covering Bjelovar Subdepression mapping area with Thiessen polygon maps of e-log markers Rs5, Z' and Δ.*

mapping of afore-mentioned e-log markers. Given method was firstly used for computing the average rainfall over given area (e.g., [13]), and has been described in detail in numerous papers (e.g., [14–17]) where a polygon of influence (known as Thiessen or Voronoi polygon) is constructed in such a way that its geometry will include all data points that are closer to the sample compared to any other measurements. These polygons (or diagrams) of influence are described by all midpoints between each neighbouring sample data [14].

Zonal estimation was done using open source software, SAGA GIS, for Thiessen polygons computation. Thiessen polygon maps (Figure 2) allowed a quick assessment of depth values over the entire mapped area, even of non-sampled areas. Each polygon has a point value that represents centre of a grid cell.

Applied Kriging techniques and results

Kriging represents an advanced statistical estimation method and one of the most common deterministic interpolation methods used to estimate the values of regionalized variables in selected points, which are assigned a relevant weighting coefficient that represents the influence of a particular data on the value of the final estimation at the selected grid node. A regionalized variable is also random variable, but where grid of point data for selected (geological) variable can (with certainty) represent a statistically fully representative sample for a particular volume (e.g. rocks) that is analysed. Kriging methods were preceded by the determination of spatial dependencies, i.e. the variogram analysis that took into account directions of observation (directional variograms), data accumulation (clusters), and in the OK local variance, which is calculated only from data within the search ellipse.

The interpolation using OK and UK techniques was done in Surfer 13, which was preceded by variogram analysis in Variowin 2.1.0., a freeware for spatial data analysis created by [18].

The Ordinary Kriging (OK) maps

OK is one of the most commonly used Kriging techniques, which premise is constant unknown mean in the local neighbourhood of each estimation point. Variogram surface map for the variable "depth" was created (Figure 3) using following parameters: lag spacing (h) = 2000 m, number of lags = 20, angular tolerance = 45°. Given map shows two axes, blue coloured primary (direction 120°–300°) and red coloured secondary (direction 30°–210°). However, the choice between primary and secondary axis could also be based on the structural map, especially if number of variogram pairs is less than 10 by each lag (e.g., [6]). In such case it is assumed that variogram axes corresponded highly with the regional structural axis of analysed structure.

Structural map of e-log marker Rs5 [6] showed unconformity on the east of the subdepression, which affected the data number and consequently made the regional range value smaller. Unconformity can be also easily seen on Thiessen polygon maps (Figure 2), where unavailable data were displayed as dark blue polygons (centroids were given value 0). Experimental variogram of the primary axis shows range value of 15000 m, which is expected since it reflects the reduction of the sedimentary basin at the end of the Lower Pannonian and at the beginning of the Upper Pannonian (i.e. transition from Paratethys into Pannonian Lake). Variogram model was approximated using spherical model with following parameters: nugget = 11200, range = 18000 m, sill = 560000 (Figure 4).

Structural map of e-log marker Z' also showed large unconformity on the eastern part [6]. It represents Upper Pannonian/Lower Pontian boundary which is a classic example of lake deposition in Croatian part of Pannonian Basin System (abbr. CPBS). It defines period of 2. transtension when huge amounts of clastites were transported by turbidites from Eastern Alps to CPBS (e.g., [2,6,19,20,21]) resulting in deposition of numerous and thicker sandstone members. Experimental variogram of

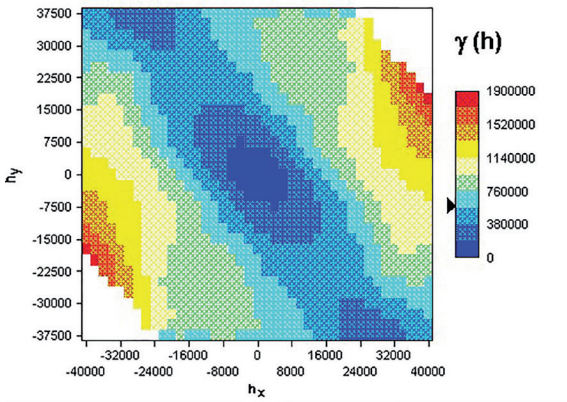

Figure 3: *The variogram surface map for variable "depth".*

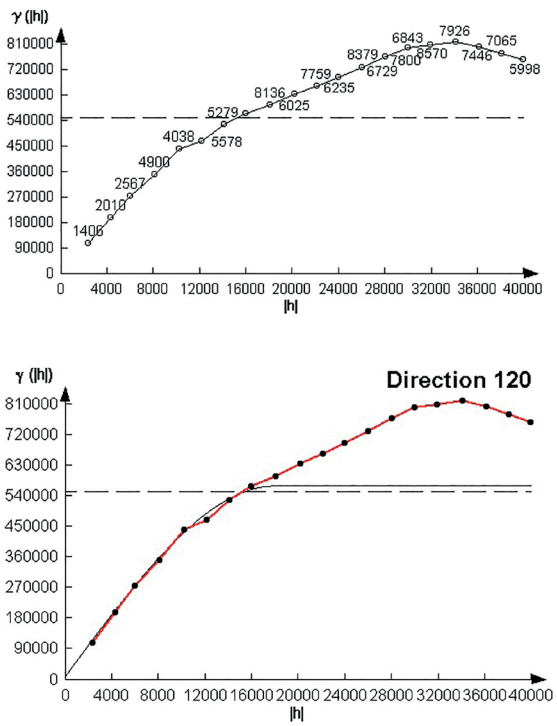

Figure 4: *Experimental variogram of the primary axis for e-log marker Rs5 (up), and corresponding theoretical spherical model (down).*

the primary axis was again approximated using spherical model with following parameters: nugget = 72000, range = 24000 m, sill = 450000 (Figure 5). A somewhat larger range is the result of the turbidity currents being the main transport mechanism at that time.

Structural map of e-log marker Δ represents transition from 2nd transtension to 2nd transpression tectonic phase [6]. The Bjelovar Sub-

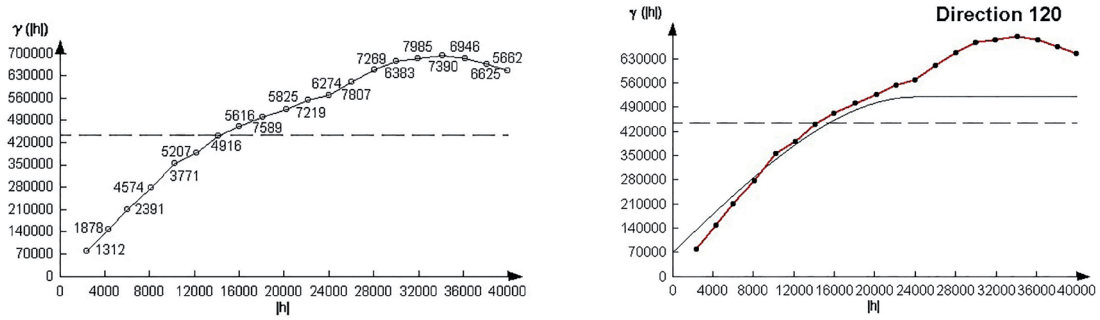

Figure 5: *Experimental variogram of the primary axis for e-log marker Z' (left), and corresponding theoretical spherical model (right).*

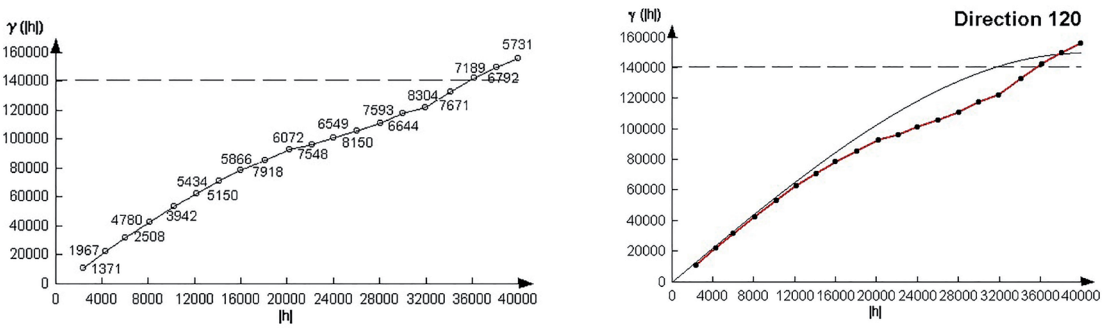

Figure 6: *Experimental variogram of the primary axis for e-log marker Δ (left), and corresponding theoretical spherical model (right).*

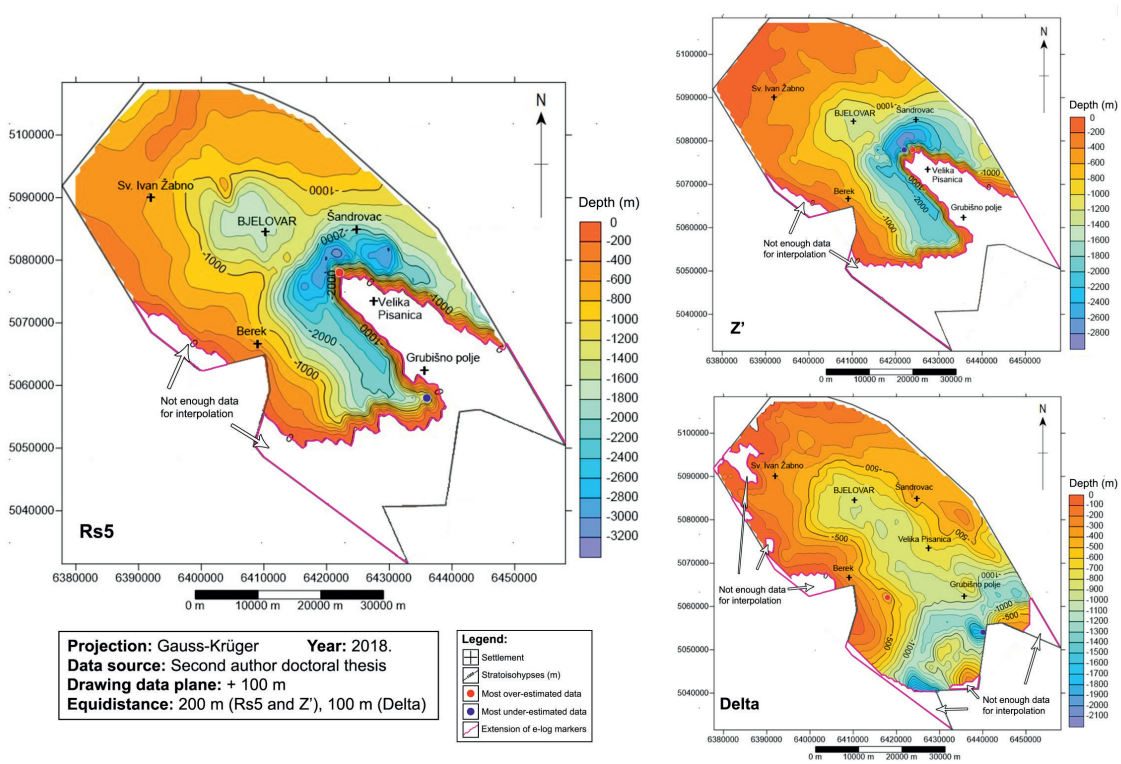

Figure 7: *The Ordinary Kriging structural maps of e-log markers Rs5, Z' and Δ.*

depression was significantly less characterised with differences among highs and lows than on deeper maps. Experimental variogram of the primary axis was, once again, approximated using spherical model with following parameters: nugget = 0, range = 40000 m, sill = 150000 (Figure 6). These are the highest range values, indicating a large spatial dependency of the data.
Figure 7 shows structural maps of e-log markers Rs5, Z' and Δ interpolated using OK technique. This set of maps had been considered as improvements regarding the previously made regional subdepressional maps interpolated by hand [2,6], but also a necessary set of OK maps that could be compared with the same UK map set, performed with the same input dataset, program and analysis (Figure 14).
As mentioned before, unconformity in the eastern part of the subdepression is easily seen on structural maps of e-log marker Rs5 and Z'. It reflects the reduction of the sedimentary basin, which caused a much smaller regional variogram range. The largest present-day depth of approximately 3000 m was recorded in the central part of the subdepression where also in past a deeper part of the lake was situated during the Pannonian/Pontian transition. On contrary, present-day margins of the subdepression, especially in the north, were shallow, or even inland. Today values at Lower/Upper Pontian border are mostly < 1000 m, with exception in the SW. Compared with previous maps, present depth values that are three times lesser, still indicating further shallowing in thepast.

The Universal Kriging (UK) maps

UK technique implies a trend in data, which in this case represents any detectable tendency for the values to change as a function of the coordinate variables. This technique assumes nonstationary regionalized variable (the mean value varies and is not constant). According to [22], it can be considered having two components: drift (average or expected value of the regionalized variable) and a residual (difference between the actual measurements and the drift). The process of using UK can be described through the following steps:

1. Understanding of trend appearance based on the nature of our data,

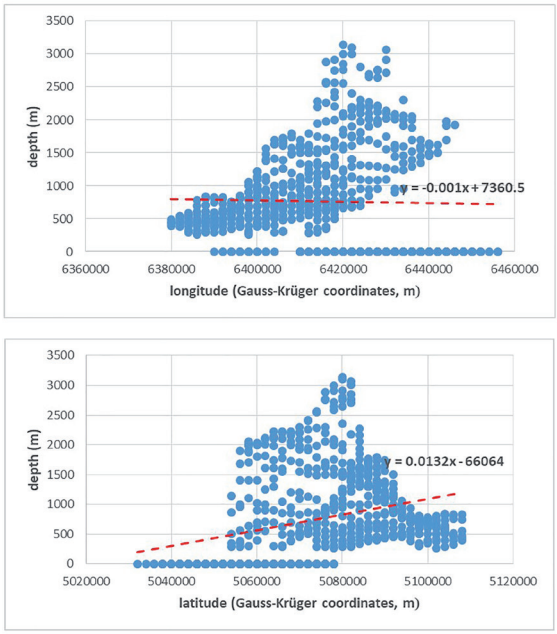

Figure 8: *Depth values read from structural map of e-log marker Rs5.*

2. Using a simple form of the trend if possible and avoiding extrapolation beyond available data,
3. Subtracting the trend from the observed data to obtain the residuals,
4. Variogram computation and spatial estimation of residuals,
5. Adding back the kriged residuals to the trend (e.g., [17]).

The spatial dependence of data can be displayed using simple scatter diagram. Figure 8 shows scatter plot with barely noticeable negative linear trend of depth with longitude and positive with latitude. It represents a set of 743 data of e-log marker Rs5. However, as mentioned before, due to large unconformity in the eastern part of the subdepression, set of 232 depth data were given value 0. If only the 511 absolute depth values were taken into consideration, Pearson's correlation coefficient of the longitude and depth is -0.35 (R^2 = 0.13), and the latitude and depth 0.66 (R^2 = 0.44), which means that the linear bond in this case is of "medium strength" (Figure 8).
Depth data set of e-log marker Z' counts 720 data points. In this case, only 497 absolute

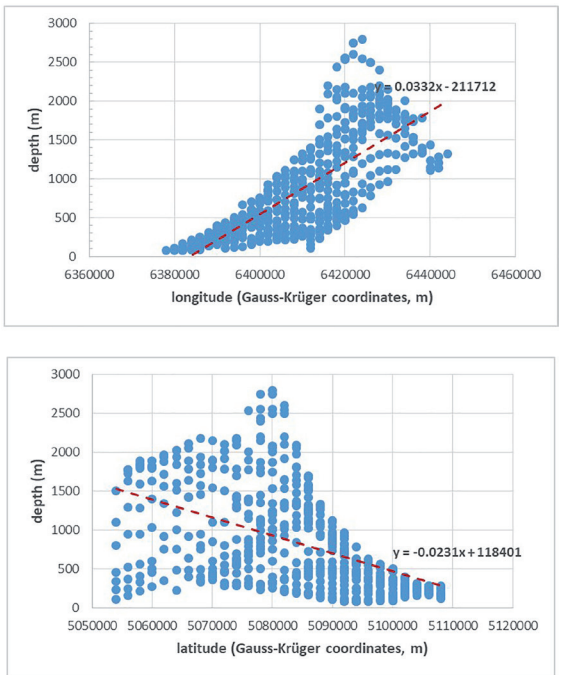

Figure 9: *Depth values read from structural map of e-log marker Z'.*

Figure 10: *Depth values read from structural map of e-log marker Δ.*

depth values read from the structural map are shown in scatter plot for a better trend view (Figure 9). The linear bond is stronger in terms of the strong linkage of the depth with the latitude where r = 0.76 (R^2 = 0.57) and with the longitude where r = -0.49 (R^2 = 0.23).

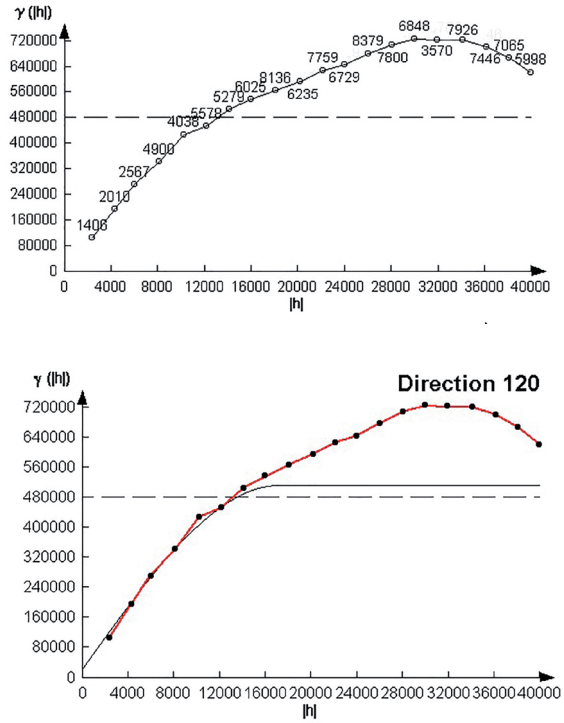

Figure 11: *Experimental variogram of the primary axis for variable "residuals" for e-log marker Rs5 (up), and corresponding spherical theoretical model (down).*

The depth values of the e-log marker Δ (set of 727 data of which 689 are absolute values) show a clear positive linear trend (Figure 10) with longitude (r = 0.68, R^2 = 0.47), and a negative with the latitude (r = -0.58; R^2 = 0.34).

After trend determination, multiple regression analysis (since there are two independent variables - longitude and latitude) is performed to obtain the variable "residuals" for the variogram computation. The result are the variograms of residuals for e-log markers Rs5, Z' and Δ that follow bellow.

Unaltered parameters of lag spacing (2000 m), number of lags (20), angular tolerance (45°), direction of primary (120°–300°) and secondary axis (30°–210°) were used. For residual data of e-log marker Rs5, experimental variogram of the primary axis was approximated using spherical model (Figure 11) with following parameters: nugget = 0, range = 17200 m, sill = 490000, where every parameter had a lower value compared to OK technique.

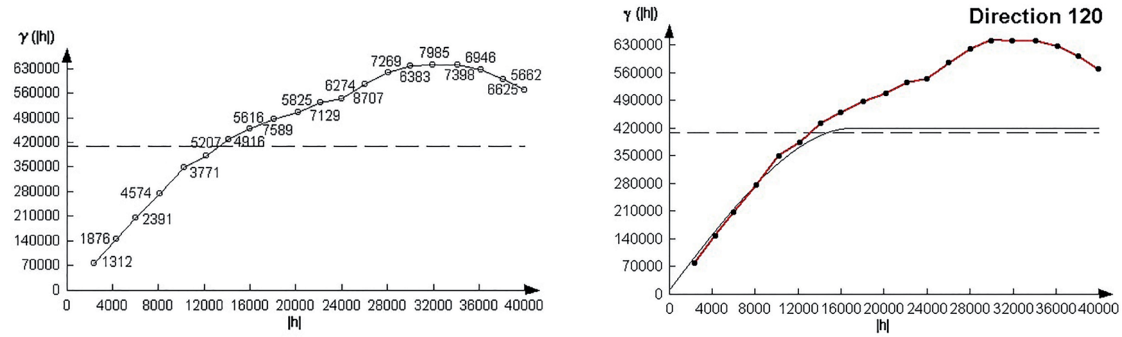

Figure 12: *Experimental variogram of the primary axis for variable "residuals" for e-log marker Z' (left), and corresponding spherical theoretical model (right).*

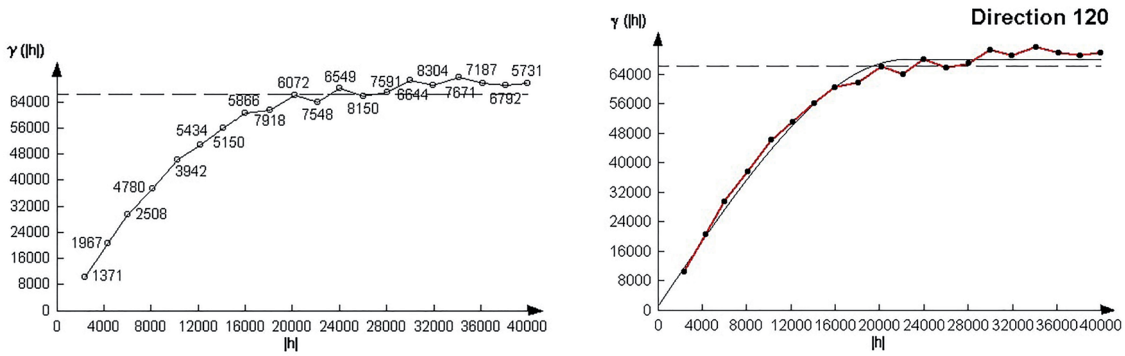

Figure 13: *Experimental variogram of the primary axis for variable "residuals" for e-log marker Δ (left), and corresponding spherical theoretical model (right).*

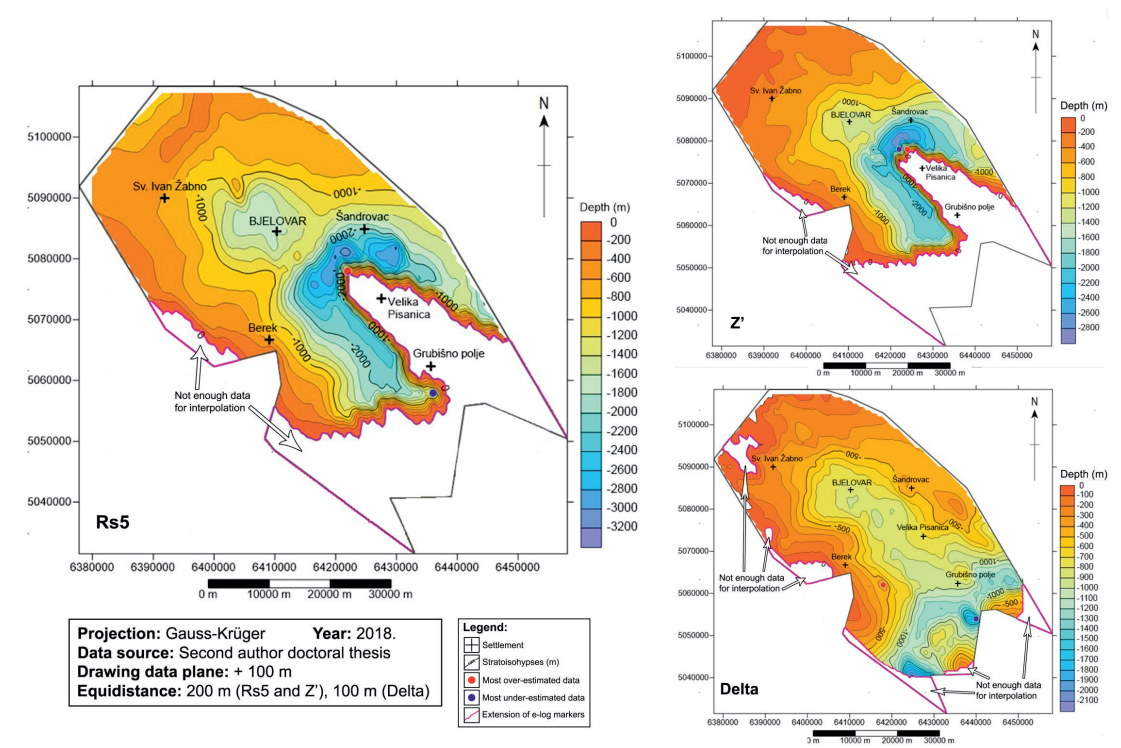

Figure 14: *The Universal Kriging structural maps of e-log markers Rs5, Z' and Δ.*

Experimental variogram of e-log marker Z' for residual data of the primary axis and its approximation with spherical models is shown in Figure 12. Range is equal to previous variogram of residual data of e-log marker Rs5 (17200 m), while the nugget is 12300, and the sill 41000.
For residual data of e-log marker Δ, experimental variogram of the primary axis was approximated using, as in all previous examples, spherical model (Figure 13). Input data for UK technique were as follows: nugget = 1340, range = 22400 m, sill = 67000.
UK map of e-log marker Rs5 (Figure 14) gives smaller crossvalidation value (RMSE = 267.9) compared to the OK map (RMSE = 268.2). Most over-estimated data is for both maps at the same coordinates (X = 6435993, Y = 5057986), where the measured value of the "depth" variable is 1880 m and the estimated value of the "depth" variable for OK amounts 157.7 m and UK 152.8 m. The same goes for most under-estimated data with coordinates at X = 6421993, Y = 5077986, where the original value of the "depth" variable is 0 m and the estimated by OK = 1568.8 m, while with UK = 1567.6 m (Figures 7 and 14).
In case of e-log marker Z', OK technique has smaller crossvalidation value (RMSE = 237.9), compared to UK (RMSE = 238.6). UK map shows identical coordinates of most over-estimated (X = 6424000, Y = 5078000) and under-estimated data (X = 6422000, Y = 5078000) as do OK map (Figures 7 and 14), next to unconformity line. Original value of most over-estimated data is 0 m, while estimation made by OK and UK is 1416.2 m and 1424.1 m. Most under-estimated data has original value of 2750 m, while OK and UK techniques made estimations of 1327.17 m and 1320.5 m.
Finally, UK map of e-log marker Δ also resulted with lesser crossvalidation value (RMSE = 79.3) compared to OK map (RMSE = 79.6), making it more appropriate method for mapping. Coordinates of most over-estimated and under-estimated data were as follows: X = 6418000, Y = 5062000 and X = 6440000, Y = 5054000 (Figures 7 and 14). Original value of the "depth" variable for most over-estimated data is 195 m, while OK and UK estimations were 543.2 m and 543 m, respectively. Most under-estimated data have original "depth" value 1800 m, but OK and UK estimations were 1286.9 m and 1285.8 m, respectively.

Discussion

Structural maps often show a trend in input data since mapped surfaces can have a structural slope towards a cardinal direction, or a number of geological structures can be part of a larger structural unit such as monocline. Therefore, with such set of data marked by a trend, it is advisable to use UK in relation to OK, because this technique was developed precisely to identify the trend in the data (in geology it is a common occurrence), calculate it, i.e. describe it with regression and ultimately do better mapping (e.g., [23]).
The UK technique is also advisable to use when the dependent variable does not meet the criteria of second order stationarity required for most of the Kriging techniques. Second order stationarity means that the middle and the variance are equal in the whole area and that the correlation between any two observations depends only on their relative position in the space. To be honest, the OK also solved such a problem in practice, using local variance for calculating each grid point applied to the applied spatial ellipsoid.
However, the main problem using the UK is size of the analysed area. Very often particular structure is characterised with easily observable geological trend, the most often structural, but sometimes also depositional. In such case, it is easy to numerically (linearly) describe such trend (like on monocline) and apply the UK.

Conclusions

Regional maps often include numerous structures, each of them characterised with own trend, but also there is one large, regional trend inherent for entire mapped area (like here subdepression). When smaller trends are easily described using regression, large trend can be masked for such type of analyses, especially if there are a few regional faults. The problem of faults is also the typical problem for interpolation software that are cell oriented algorithms

that try smoothly change values among neighbourhood cells (vs. abrupt fault throws).
For this reason, within the Bjelovar subdepression area, the UK and OK give similar crossvalidation values since faults break the trend in the data, i.e. on the subdepression kilometre-scale, with several regional faults, it is almost impossible to determine a regional trend (i.e. there are more). Hence, the UK's higher accuracy in relation to OK is on a smaller surface, as it was in the example of the Šandrovac field (e.g., [12]). On the contrary, a whole set of structural maps interpolated using OK technique at the subdepression level could not be improved by simply re-mapping this area with the UK technique.
However, thanks to the more advanced UK algorithm and very detailed set of structural and thickness maps made in the past, at the level of two e-logs, where the depth differences between the individual structures were not so great and the throws were mostly gradual, the UK technique resulted in the best structural maps made so far (of e-log markers Rs5 and Δ). In addition, for such datasets also now exists the new variogram models, which included data residuals. And last, here is shown the advantage of Thiessen polygons as introductory analysis that could precede Kriging interpolation on regional scale. Using such polygons, the geologist can easily recognise the regional trends if exist as well as zones where value transitions could be too large on close distances that regional trends could be meaningful to analyse.

Acknowledgment

This work represents part of doctoral researching of Dr. Ivana Mesić Kiš. Partially, it was also done by financial supports „Mathematical methods in geology II and III" given by University of Zagreb, Faculty of Mining, Geology and Petroleum Engineering in 2017 and 2018.

References

[1] Vukotinović, L. (1852): Kamenopisna slika gore Moslavačke (Geological sketch of Moslavačka Mt.). Available at https://www.krizevci.eu/hr_HR/slika/licnosti/vukotinovic/kamenopis.jpeg.

[2] Malvić, T. (2003): *Naftnogeološki odnosi i vjerojatnost pronalaska novih zaliha ugljikovodika u Bjelovarskoj uleknini (Oil-Geological Relations and Probability of Discovering New Hydrocarbon Reserves in the Bjelovar Sag),* Ph. D. Thesis. Zagreb: University of Zagreb, Faculty of Mining, Geology and Petroleum Engineering; 123 p.

[3] Malvić, T., Rusan, I. (2007): Potential Hydrocarbon Discoveries in Bjelovar Subdepression, Croatia. *Search and Discovery, 9*, 10133, pp. 1–6.

[4] Malvić, T., Sučić, A., Cvetković, M., Resanović F., Velić, J. (2014): Low permeability Neogene lithofacies in Northern Croatia as potential unconventional hydrocarbon reservoirs. *Central European Journal of Geosciences,* 6(2), pp. 182–194.

[5] Mesić Kiš, I. (2017): *Kartiranje i reinterpretacija geološke povijesti Bjelovarske subdepresije univerzalnim krigiranjem te novi opći metodološki algoritmi za kartiranje sličnih prostora (Mapping and reinterpretation of the geological evolution of the Bjelovar Subdepression by Universal Kriging and new general methodological algorithms for mapping in similar areas),* Ph. D. Thesis. Zagreb: University of Zagreb, Faculty of Science; 182 p.

[6] Malvić, T. (2011): Geological maps of Neogen sediments in the Bjelovar Subdepression (northern Croatia). *Journal of Maps, 7*(1), pp. 304–317.

[7] Špelić, M., Malvić, T., Saraf, V., Zalović, M. (2016): Remapping of depth of e-log markers between Neogene basement and Lower/Upper Pannonian border in the Bjelovar Subdepression. *Journal of Maps,* 12(1), pp. 45–52.

[8] Malvić, T., Đureković, M. (2003): Application of the methods: Inverse distance weighting, ordinary kriging and collocated cokriging in porosity evaluation, and comparison of results on the Beničanci and Stari Gradac fields in Croatia. *Nafta,* 54(9), pp. 331–340.

[9] Balić, D., Velić, J., Malvić, T. (2008): Selection of the most appropriate interpolation method for sandstone reservoirs in the Kloštar oil and gas field. *Geologica Croatica,* 61(1), pp. 23–75.

[10] Malvić, T. (2008): *Primjena geostatistike u analizi geoloških podataka (Application of geostatistics in geological data analysis)*. University literature, INA Plc., Zagreb, 103 p.

[11] Husanović, E., Malvić, T. (2014): Review of deterministic geostatistical mapping methods in Croatian hydrocarbon reservoirs and advantages of such approach. *Nafta,* 65(1), pp. 57–63.

[12] Mesić Kiš, I. (2016): Comparison of Ordinary and Universal Kriging interpolation techniques on a depth

variable (a case of linear spatial trend), case study of the Šandrovac Field. *Rudarsko-geološko-naftni zbornik,* 31(2), pp. 41–58.

[13] Thiessen, A.H., (1911): Precipitation for large areas. *Monthly Weather Review,* 39, pp. 1082–1084.

[14] Chow, V.T., (1964): *Handbook of applied hydrology: A compendium of water-resources technology.* New York: McGraw-Hill, 1468 p.

[15] Brassel K.E., Reif D. (1979): A Procedure to Generate Thiessen Polygons. *Geographical Analysis,* 11(3), pp. 289–303.

[16] Boots, B.N. (1987): Modifying Thiessen Polygons. *The Canadian Geographer,* 31(2), pp. 160–169.

[17] Isaaks, E., Srivastava, R. (1989). *An Introduction to Applied Geostatistics*. New York: Oxford University Press Inc., 561 p.

[18] Pannatier, Y. (1996): *VARIOWIN – Software for spatial data analysis in 2D*. New York: Springer, 91 p.

[19] Malvić, T. (2012): Review of Miocene shallow marine and lacustrine depositional environments in Northern Croatia. *Geological Quarterly,* 56(3), pp. 493–504.

[20] Malvić, T. (2016): Regional turbidites and turbiditic environments developed during Neogene and Quaternary in Croatia. *Materiali in geokolje (Materials and geoenvironments),* 63, pp. 39–54.

[21] Malvić, T., & Velić, J. (2011): Neogene tectonics in Croatian Part of the Pannonian Basin and Reflectance in Hydrocarbon Accumulations. Proceedings "*New Frontiers in Tectonic Research: At the Midst of Plate Convergence*" (Ed., Schattner, U.), InTech, 215–238, Rijeka.

[22] Davis, J.C. (1973). *Statistics and Data Analysis in Geology*. New York: Wiley, 550 p.

[23] Veronesi, F. (2012): *3D Advanced mapping of soil properties*. Ph. D. Thesis. Bedford: Cranfield University 2012; 159 p.

Original scientific paper

Received: Jan 27, 2018
Accepted: Aug 15, 2018
DOI 10.2478/rmzmag-2018-0017

Preliminary geophysical investigation for road construction using integrated methods

Predhodne geofizikalne raziskave tal pri gradnji cest z uporabo korelacijskih metod

Joel Olayide Amosun[1]*, Gbenga Moses Olayanju[2], Oluseun Adetola Sanuade[1], Tokunbo Fagbemigun[1]

[1] Department of Geophysics, Federal University Oye-Ekiti, Ekiti State, Nigeria.

[2] Department of Applied Geophysics, Federal University of Technology Akure, Ondo State, Nigeria.

* joelamosun@gmail.com

Abstract

Integrated geophysical methods have been used to investigate the competency of the subsoil. The geophysical surveys conducted involve very low-frequency electromagnetic (VLF-EM) and electrical resistivity (ER) methods (dipole–dipole). ABEM Wadi and Ohmega resistivity meter were used to acquire VLF-EM and ER data, respectively, along two traverses. Station interval of 5 m was used for the VLF-EM survey, while inter-electrode spacing for dipole–dipole was 10 m; the inter-dipole expansion factor (*n*) ranged from 1 to 5. KHFFILT software was used to generate VLF-EM profiles and pseudosection, while DIPRO software was used for ER. Results from the ER method revealed the pattern of resistivity variations within the study area. The low resistivity values (11–25 Ohm-m) observed at the southern part of the study area could be attributed to changes in clay contents and degree of weathering in the subsurface. The results from the VLF-EM investigation revealed the presence of near-surface linear geologic structures of varying lengths, depths and attitudes, which suggest probable conductive zones that are inimical to the foundation of the road subgrade.

Key words: Electrical resistivity, roadway subgrade, subsoil competence, clay material, road failure

Povzetek

Primernost globlje plasti tal za cestogradnjo smo preiskali s kombinacijo geofizikalnih metod. Uporabili smo zelo nizkofrekvenčne elektromagnetne (VLF-EM) in električne upornostne (dipolno-dipolne) postopke. Elektromagnetne in električne upornostne podatke smo izmerili po dveh profilih z opremo ABEM WADI in Ohmega merilcem upornosti. Preiskavo VLF-EM smo opravili ob 5-metrskem razmaku med postajama, medelektrodni dipolno-dipolni razmak je bil 10 m, znotraj dipolni ekspanzijski faktor (*n*) pa med 1 in 5. Za izdelavo elektromagnetnih profilov in psevdopresekov smo uporabili programsko opremo KHFFILT, za električno upornost pa opremo DIPRO. Rezultati so razkrili nekaj različnih vzorcev porazdelitve upornosti na proučevanem terenu. Nizke vrednosti upornosti (11-25 Ohm-m) v južnem delu preiskovanega ozemlja kaže pripisati spremembam vsebine gline in različni stopnji preperelosti tal. Rezultati elektromagnetne preiskave pričajo o navzočnosti blizupovršinskih linearnih geoloških struktur različne dolžine, globine in zaleganja, kar nakazuje verjetne prevodnostne cone, ki niso ugodne za izdelavo obstojne cestne podgradnje.

Ključne besede: električna upornost, cestna trasa, primernost tal, glinena zemljina, nezanesljivost podlage

Introduction

Road failure constitutes a major problem in most part of the world. Most Nigerian roads fail immediately after construction and even before their design age. Some of the factors responsible for these road failures are poor construction materials, bad design, poor drainage network, geological factors, abandon river channels, high water table, water flooding and fallen tree trunks that were left and buried [1–5]. However, geological factors are rarely considered as one of the factors responsible for such failures even though these roads are built on the soil. This shows that road construction requires adequate knowledge of the conditions of subsurface [6]. The non-consideration of geologic factors has led to many road and highway failures in the country. Previous studies have shown that the integrity of roads can be undermined by the existence of geological features as well as the engineering characteristics of the underlying geologic sequences [7–14]. However, there is need to carryout pre-construction geophysical investigation prior to road construction. Therefore, this study aims to investigate the significance of geological factors in terms of the nature of the subsoil, near-surface structures and the bedrock structural disposition as possible causes of road failures at Aule along Ilesa Garage, Ondo State, Nigeria, using geophysical investigations.

Description and geology of the study area

The study area is located in Aule in Akure South local government area of Ondo State, Nigeria. The study area falls within latitude 7°16′20″N–7°16′30″N and longitude 5°9′5″E–5°9′20″E (Figure 1). The study area lies within the Precambrian basement complex of Southwestern Nigeria. The Precambrian rocks of the region may be separated into three major petro-lithologic units, which are reactivated basement complex of gneisses and migmatites; the schist belt, which predominantly comprises supracrustal rocks occurring within northerly trending trough in the basement complex and the Pan African older granite series, a suite of granites and related rocks that intrude the above successions [15]. However, the main rock type found in the study area is migmatite–gneiss (Figure 2).

Methodology

Geophysical investigation involving the integration of very low-frequency electromagnetic (VLF-EM) and electrical resistivity (ER) methods was carried out along traverses in the area. Only survey for traverse 1 was carried out for both VLF-EM and ER, and detailed correlation between two methods is presented. However, due to inaccessibility to the road at the time of conducting measurements, only the ER method for traverse 2 was established. The ER method used dipole–dipole array using Ohmega resistivity meter. Basically, the ER method involves the passage of electric current using DC or low-frequency AC into the subsurface through two electrodes, that is, the current electrodes. The potential difference is measured between another pair of electrode, which may or not be within the current electrodes depending on the electrode array in use. The inter-electrode spacing used was 10 m, and the inter-dipole expansion factor (n) ranged from 1 to 5. ABEM Wadi was used for the VLF-EM acquisition. The VLF-EM method is an inductive exploration technique that is used in mapping shallow subsurface structural features in which the primary EM wave induces current flow. Although both the real and quadrature components of the VLF-EM were measured, the real component data, which are usually diagnostic of linear features, were processed for qualitative interpretation. VLF transmitter operating at a frequency of 18.9 kHz was used. The station-to-station interval of 5 m was adopted for the survey, and data were acquired along the established two traverses.

The resistivity data were processed using *DIPRO* software [17] to obtain 2-D pseudosections. The real and the filtered components of the VLF-EM data were plotted against station using the *KHFFILT* software [18] and were presented as profiles.

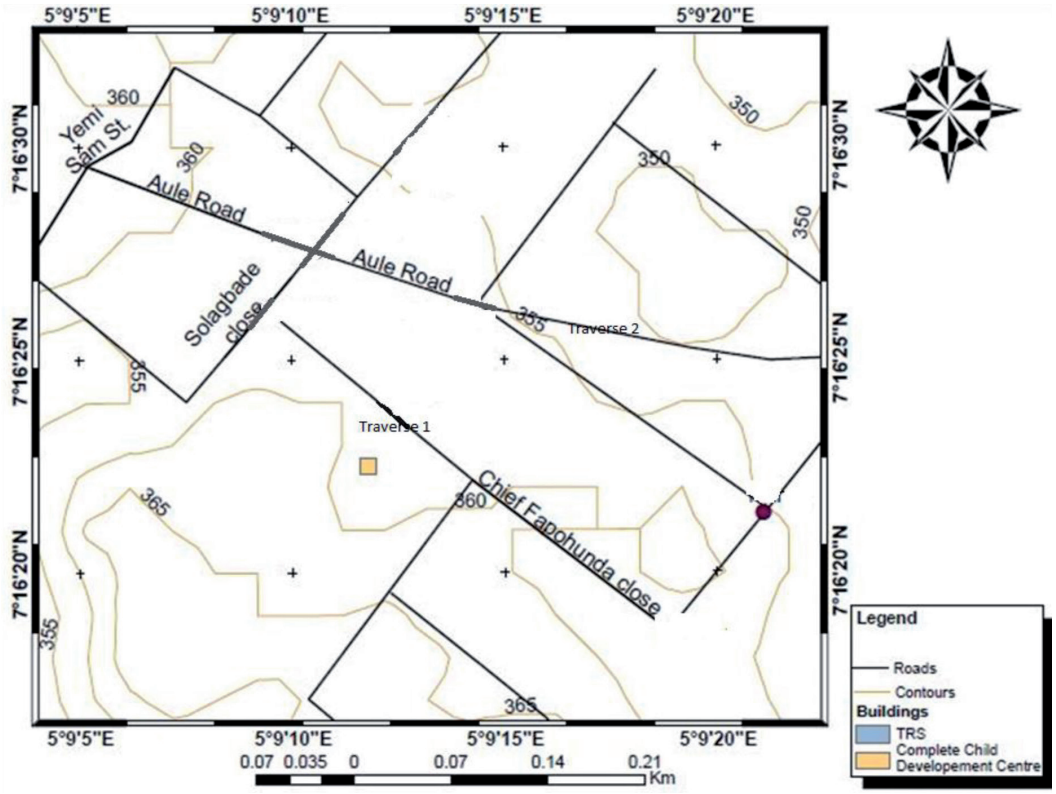

Figure 1: *Location map of the study area and its environs.*

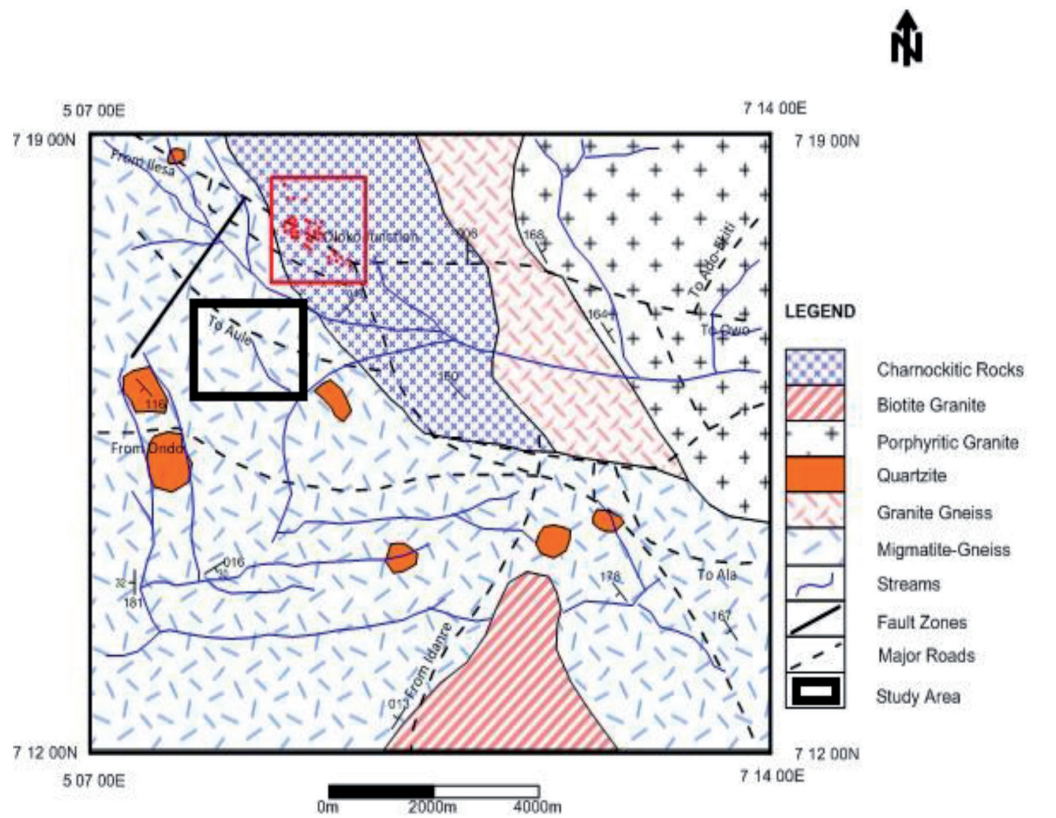

Figure 2: *Geological map of Akure (modified after [16]).*

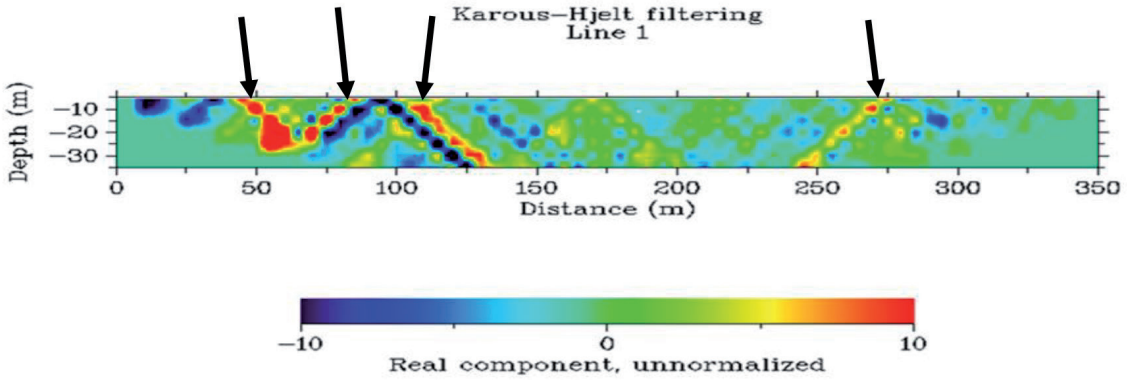

Figure 3: *2-D VLF-EM subsurface conductivity image for traverse 1.*

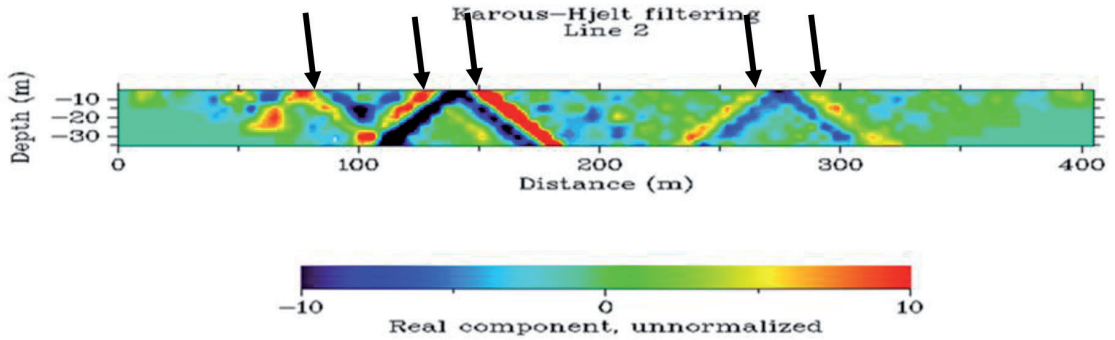

Figure 4: *2-D VLF-EM subsurface conductivity image for traverse 2.*

Results and discussion

The VLF-EM Profiles

Figure 3 shows suspected geologic features such as fault or fracture having varying degrees of conductivity as indicated by arrows on the section. Between distance 40 and 80 m, the resistivity is low, depicting a conductive body to a depth of about 10 m. Similarly, between distance 125–132 m and 180–200 m, a conductive body that orientate towards the northern part of the section at a depth exceeding 12 m is observed. In adddition, towards the northern part of the section is a conductive body at a distance between 240 and 250 m. However, two prominent high conductive zones were found at different points between 50–100 m and 250–275 m as shown in Figure 3.

Figure 4 shows similar structures such as fault or fracture along traverse 2. There are features of different degrees of conductivities on the section, while at distance between 150 and 200 m, a conductive zone is observed (low resistivity). At a distance between 5 and 35 m, a resistive body is observed, which may be as a result of an outcrop closer to the location. There is a presence of a highly conductive body between station distance 220 and 240 m, indicative of an incompetent layer across the road segment.

ER pseudosection

The inverted section in Figure 5 shows that between stations 32 and 111, there is a layer of low resistivity (having values ranging from 11 to 35 Ohm-m) at depth of 1–10 m. The shape of the material suggests the presence of pocket of clay materials at these locations. There is also a resistive layer between stations 115 and 217, which is about 1–8 m thick. At stations 21–51 of the section, there is a layer of relatively thin resistive material as the topsoil, which may be an indication of the topsoil compaction along the road segment. At stations 301–321, the resistivity value is between 14 and 21 Ohm-m, indicating clayey materials. This region also shows high conductive layers between stations 111–121

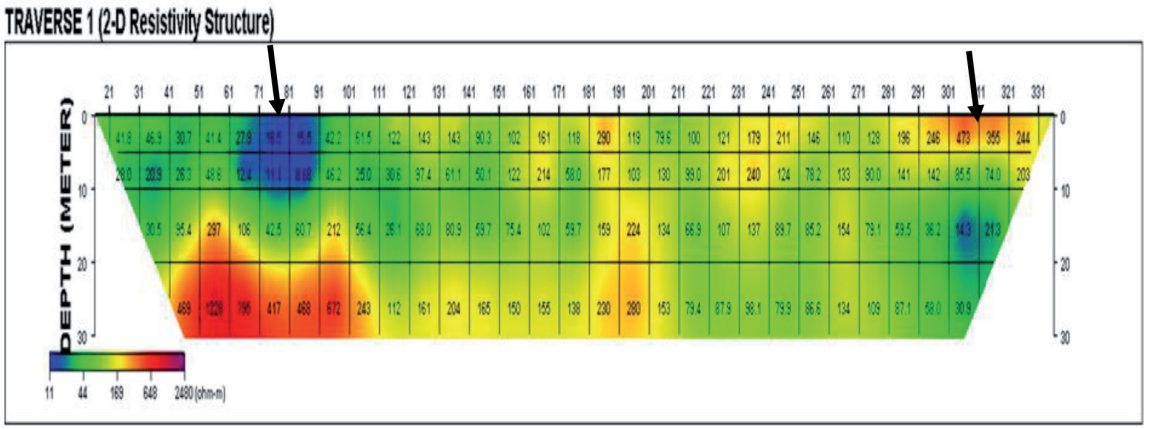

Figure 5: *The inverse model resistivity section for traverse 1.*

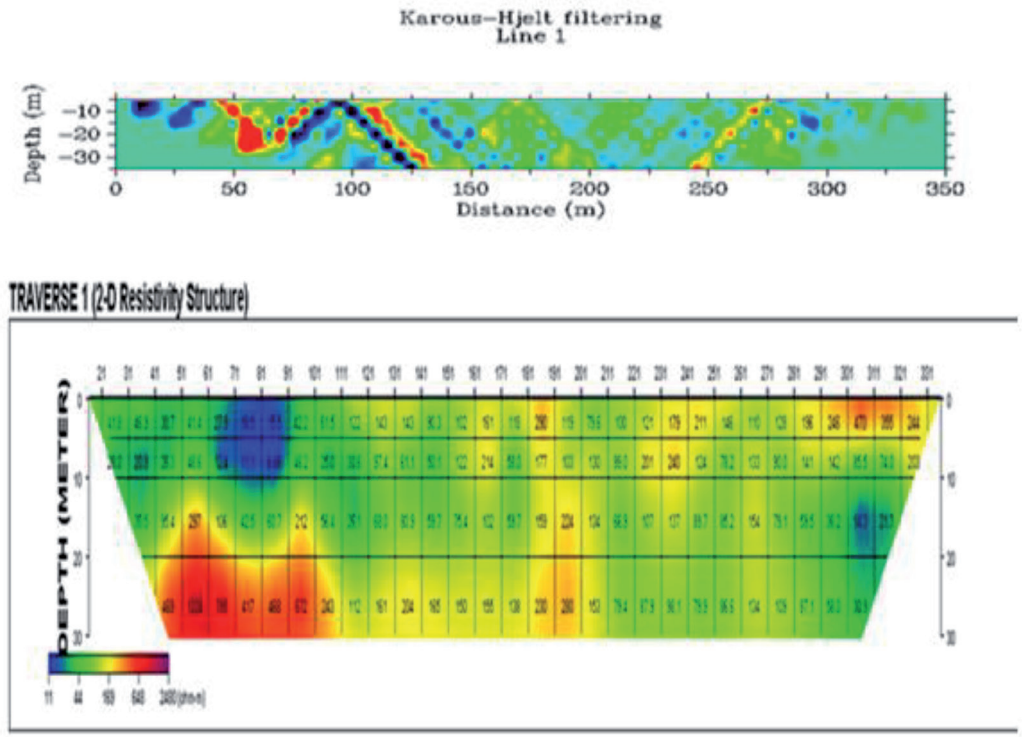

Figure 6: *Correlation between conductive VLF-EM and dipole–dipole resistivity survey for traverse 1.*

and 301–321 along the profile due to their relative low resistivity, indicating high saturation in the region [19]. The relatively high-resistivity anomalies observed at the depth of about 4 m at the southern part of the section between stations 41 and 105 show that the subsurface materials in this region are highly resistive. The topsoil is conductive between stations 1 and 91, depicting clayey material, although there is decrease in clay material between stations 101 and 331 with thick overburden. The correlation between VLF profile and pseudosection resistivity for traverse 1 (Figure 6) shows that the principal geologic features that could pose a threat to the road construction in the study area is found at distance between 40 and 80 m in traverse 1 and stations 60 and 91 in the inverse model resistivity section, which could be a pocket of clay material.

Conclusions

Integrated geophysical methods have been used to investigate the subsoil competency along Aule–Akure road, Ondo State, Southwestern Nigeria. The results show that there is a pattern of resistivity variations within the study area. The low resistivity anomalies observed along the traverses could be due to changes in moisture contents or the point being a water collection centre, which could cause the topsoil to be incompetent.

The results also indicate the clayey nature of the topsoil/subgrade soil on which the road pavement could be established. Clay, although highly porous but less permeable owing to poor connectivity of its pores, retains water without releasing it, thus making it swell and this subsequently will lead to road failure. The presence of near-surface linear features such as faults, fractured zones, fissures and joints in the subsoil beneath the road pavement could cause pavement failure.

Therefore, proper drainage pattern should be constructed between traverses 1 and 2 in order to discourage the accumulation of runoff and thereby expose the subsurface material to erosion and lead to incompetency of the investigated area, and the excavation of the clay material established should be carried out at a depth of about 4 m and be replaced by more competent geologic material before the construction of road.

References

[1] **Adiat, K.A.N, Adelusi, A.O., Ayuk, M.A. (2009).** Relevance of Geophysics in Road Failures investigation in a typical basement complex of southwestern Nigeria. Pacific Journal of Science and Technology 5(1): 528–539**.**

[2] **Akintorinwa, O.J., Ojo, J.S., Olorunfemi, M.O. (2010).** Geophysical investigation of pavement failure in a basement complex terrain of south-western Nigeria. Pacific journal of science and technology 11(2): 649–663.

[3] **Momoh, L.O., Akintorinwa, O.J., Olorunfemi, M.O. (2008).** Geophysical Investigation of Highway Failure. A case Study from the Basement Complex Terrain of South-western Nigeria. Journal of Applied Sciences Research 4(6): 637–648.

[4] **Omujakporue, O.G (2012).** Geophysical Investigation of the Causes of Highway Failures in Niger Delta Sedimentary Basin (A Case Study of the Eastern Part of East-West Road), Nigeria. Scientia Africana 11(1): 143–152.

[5] **Oni, A.G., Olorunfemi, M.O. (2016).** Integrated Geophysical Investigation of the Igbara-Oke-Igbara-odo Road Pavement Failure in Ondo/Ekiti State, Southwestern Nigeria. Ife Journal of Science 18(1): 119–131.

[6] **Nwokoma, E.U., Chukwu, G.U., Amos-Uhegbu, C. (2015).** Geoelectrical Investigation of Soils as Foundation Materials in Umudike Area, Southeastern Nigeria. Physical Science International Journal 6(2): 82–95.

[7] **Adeleye, A.O. (2005).** Geotechnical Investigation of Subgrade Soil along Sections of Ibadan-Ife Highway. Unpublished M.Sc. Project, Obafemi Awolowo University; 181Pp.

[8] **Farinde, M.A., Oni, S.O. (2015).** Geophysical and Geotechnical Characterization of Newly Constructed Abadina-Ajibade Road, University of Ibadan, Ibadan. Journal of Multidisciplinary Engineering Science and Technology 2(1): 363–378.

[9] **Mesida, E.A, (1987).** The Relationship between the Geology and the Lateritic Engineering Soils in the Northern Environs of Akure, Nigeria. Bulletin of the International Association of Engineering Geology 35: 65–69.

[10] **Olorunfemi, M.O., Ojo, J.S., Sonuga, F.A., Ajayi, O., Oladapo, M.I (2000).** Geoelectric and Electromagnetic Investigation of the field Koza and Nassarawa Earth Dams around Katsina, Northern Nigeria. Journal of Geology and Mining Research 36(1): 51–65.

[11] **Olorunfemi, M.O., Ojo, J.S., Idomigie, A.I., Oyetoran, W.E (2005).** Geophysical Investigation of Structural Failure at a Factory Site in Asaba Area, Southern Nigeria. Journal of Geology and Mining Research 41(1): 111–121.

[12] **Osinowo, O.O., Akanji, A.O., Akinwosin, A. (2011).** Integrated Geophysical and Geotechnical Investigation of the Failed Portion of a Road in Basement Complex Terrain, southwestern Nigeria. RMZ- Material and Geoenvironment 58(2): 143–162.

[13] **Oladunjoye M.A., Salami A.J., Aizebeokhai A.P., Sanuade O.A., and Kaka S.I. (2017).** Preliminary geotechnical characterization of a site in Southwest Nigeria using integrated electrical and seismic methods. Journal Geological Society of India 89: 209–215.

[14] **Oyeyemi K.D., Aizebeokhai A.P., Adagunodo T.A., Olofinade O.M., Sanuade O.A, Olaojo A.A. (2017).** Subsoil characterization using geoelectrical and geotechnical investigations: Implications for foundation studies. International Journal of Civil Engineering and Technology 8(10): 302–314.

[15] **Obaje, N.G (2009).** Geology and Mineral Resources of Nigeria. Heidelberg: Springer, 221p.

[16] **Owoyemi, F.B. (1996).** A geologic-Geophysical Investigation of Rain-induced erosional features in Akure Metropolis. Unpublished M.Tech Thesis, Federal University of Technology Akure, pp. 11–18.

[17] **DIPRO (2000).** DIPRO for Windows Version 4.0 Processing and Interpretation Software for Diole-Dipole Electrical Resistivity Data. KIGAM, Daejon, South Korea.

[18] **Karous, G.V., Hjelt, S.E. (1983).** Linear-filtering of VLF Dip-angle measurements. Geophysical Prospecting 31: 782–894.

[19] **Bayewu, O.O., Mosuro, G.O., Oloruntola, M.O., Osho, A.C. (2012).** The Resistivity and Electromagnetic Survey for Groundwater Evaluation in Part of Ago-Iwoye, Southwestern Nigeria. International Journal of Advances in Science and Technology 5(1): 77–99.

Original scientific paper

Received: Nov 15, 2017
Accepted: May 28, 2018
DOI 10.2478/rmzmag-2018-0018

Geochemical assessment of claystone deposits from the Patti Formation, Southern Bida Basin, Nigeria

Geokemična opredelitev plasti glinavca formacije Patti v južni kadunji Bide v Nigeriji

Ohanyiri C. Chiemezie*, Omotowo B. Aminat
Department of Geology, University of Ibadan, Ibadan, P.M.B. 5116, Oyo State, Nigeria
* emezieohans@gmail.com

Abstract

Geochemical studies of claystone deposits from the Patti Formation in the southern Bida Basin, north-Central Nigeria, were carried out on representative samples to determine the basin's depositional conditions, provenance and tectonic setting. The localities within the study area included Gegu, Ahoko, Ahoko-Etigi, Omu and Idu.

Semi-quantitative phase analysis using the Rietveld method and X-ray powder diffraction data revealed that the claystone samples had prominent kaolinite with other constituents such as quartz, illite–muscovite, K-feldspar, pyrite, marcasite, anatase, rutile and gorceixite.

Enrichment of Al_2O_3, Ba, Th, Sr, Cr and La suggests that these elements are primarily controlled by the dominant clay minerals.

Geochemical parameters such as U, U/Th, Ni/Co, V/Cr and Cu/Zn ratios strongly implied that these claystones were deposited in an oxidising environment. Provenance deducing ratios for felsic, mafic and basic igneous rocks were compared. Al_2O_3/TiO_2 ratio suggested intermediate to felsic rocks as the probable source rocks for the claystone samples; however, Y/Ni, Cr/V, La/Sc and Th/Sc ratios suggested a felsic progenitor. The tectonic discrimination diagram showed that the samples' plot was within the region specified for passive margin-type tectonic setting.

Key words: claystone, geochemical, tectonic, provenance, paleo-oxygenation

Povzetek

Geokemične raziskave plasti glinavca formacije Patti v južni kadunji Bida v severnem delu osrednje Nigerije smo izvedli na reprezentativnimh vzorcih z namenom ugotoviti sedimentacijske razmere v kadunji, izvor snovi in tektonsko lego. Večji kraji v proučevanem ozemlju so Gegu, Ahoko, Ahoko-Etigi, Omu in Idu.

Semikvantitativna analiza z Rietveldovo metodo in rezultati praškovne rentgenske difrakcije pričajo o prevladujočem kaolinitu v vzorcih glinavca in o prisotnosti nadaljnjih mineralov, kot so kremen, illit-muskovit, kalijev glinenec, pirit, markazit, anataz, rutil in gorceixit.

Obogatitve Al_2O_3, Ba, Th, Sr, Cr in La nakazujejo, da so vsebine teh prvin odvisne predvsem od prevladujočih glinenih mineralov.

Geokemični parametri kot U in razmerja U/Th, Ni/Co, V/Cr in Cu/Zn pričajo o tem, da so bili glinavci odloženi v oksidnem okolju. Primerjali smo razmerja, ki nakazujejo izvorne magmatske kamnine. Razmerje Al_2O_3/TiO_2 kaže, da so matične kamnine glinavcev prehodne do felzične magmatske kamnine, Y/Ni, Cr/V, La/Sc in Th/Sc pa nakazujejo felzični izvor. Vzorčne točke, nanešene v tektonskem diskriminacijskem diagramu, so na področju značilnem za tektonsko lego tipa pasivnega roba.

Ključne besede: glinavec, geokemija, tektonska lega, izvor, paleo-oksidacijske razmere

Introduction

Claystone is a fine grained, dark grey to pink sedimentary rock mainly consisting of compacted and hardened clay. According to Gary [1], if it can be determined that most of the particles of a rock (over two-thirds) are clay sized, the rock may then be called a claystone.

Geochemical parameters have been used by several authors to decipher paleo-oxygenation conditions of ancient sediments [2–7]. Redox parameters such as Cu/Zn ratio was proposed by Hallberg [8], while U/Th ratio was proposed by Jones and Manning [3]. Hayashi et al. [9] noted that Al_2O_3/TiO_2 ratio is essentially used to infer source rock composition with various ranges given for mafic, intermediate and felsic igneous rocks.

On the basis of mean crustal abundance, geological elements are classified as major, minor and trace elements based on their percentage composition by mass in rocks. Some researchers noted that major element geochemistry of sedimentary rocks is more important in discriminating tectonic setting [10–11]; however, trace elements are more useful in discriminating tectonic evolution of rocks and the provenance of clastic materials [12]. Gritty et al. [13] attributed this to their low mobility during sedimentary depositional processes.

This study aimed at identifying the depositional environment, provenance and tectonic setting of the claystones of the Patti Formation, southern Bida Basin, North-Central Nigeria, using major and trace element geochemistry as well as clay speciation analysis.

Geology and stratigraphy

The Bida Basin as depicted in Figure 1 is a linear northwest–southeast trending intracratonic sedimentary basin extending from Kontagora in the Niger State of Nigeria to areas slightly beyond Lokoja in the south and is approximately perpendicular to the Benue Trough. It is delimited in the northeast and southwest by the basement complex, while it merges with Anambra Basin (in the north) and Sokoto Basin (in the south) in sedimentary fill comprising post-orogenic molasse facies and few thin unfolded marine sediments. The basin is frequently regarded as the north-western extension of the Anambra Basin [14–16], both of which were major depocentres during the third major transgressive cycle of southern Nigeria in Late Cretaceous time.

Adeleye [17] noted that the basin is a gently downwarped trough whose genesis may be closely connected with the Santonian orogenic movements of southeastern Nigeria and the Benue valley nearby, while Whiteman [14] and Okunlola and Olubunmi [18] suggested that the basin was formed from simple cratonic sag. Agyingi [19] proposed a post-Santonian origin for the basin stating that the sediments in the basin were generally undisturbed as in the case of the post-Santonian sediment of the adjacent Sokoto Basin and Anambra Basin.

Two main rock types found in the Bida Basin include crystalline basement rock and sedimentary rock. The crystalline rock that includes gneiss, granite, marble and quartzite are of Precambrian to early Palaeozoic age [20].

Adeleye and Dessauvagie [21] specified that overlying the basement complex are poorly exposed basal beds of coarse conglomerate and cross-stratified sandstones with angular pebbles. Conformably, overlying these basal beds are continental sediments mainly comprising sandstones, siltstones and claystones. Often, experts working in the area have divided the basin geographically into northern and southern Bida Basin [19, 22, 23], probably due to rapid changes in facies across the basins. The southern Bida Basin comprises the basal Campanian Lokoja Formation (mainly conglomerate and sandstone), Maastrichtian Patti Formation (shale, claystone and sandstone) and the youngest Agbaja Formation (ironstone). Their lateral stratigraphic equivalents in the northern Bida Basin consist of the basal Bida Formation (conglomerate and sandstone), Enagi Formation (siltstone, claystone and sandstone) and Batati Formation (ironstone) as exemplified in Figure 2. The present study correlates with the Enagi Formation.

Prominent features and structures in the basin include unconformity surfaces (nonconformity), different forms of beddings (parallel beddings, cross beddings and graded beddings), deformation, diagenetic features and fractures.

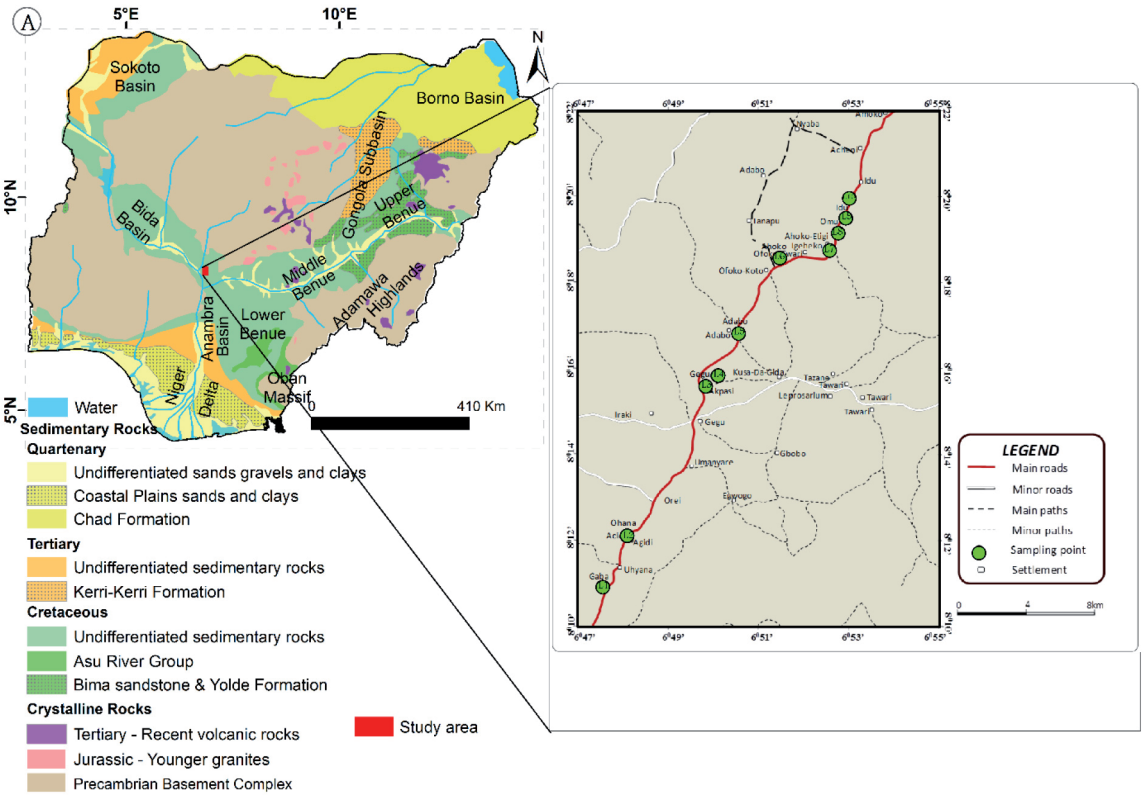

Figure 1: *Generalised geologic map of Nigeria showing sampling locations (modified after Adelana et al. [25] and Fagbohun et al. [26]).*

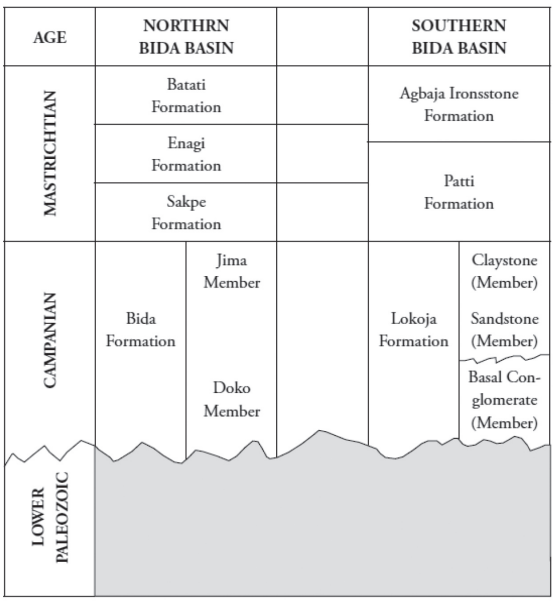

Figure 2: *Stratigraphic successions in the mid-Niger Basin (adapted from Akande et al. [16]).*

Initial gravity studies in the Bida Basin by Ojo [24] put the maximum thickness of the sedimentary successions at about 3.500 m in the central axis, while Agyingi [19] from aeromagnetic interpretation recorded a maximum sedimentary thickness of about 3.300 m.

Data and methods

The field investigation was carried out on exposed clay sections cut open by the Lokoja–Agbaji road with an effort made to obtain fresh samples for laboratory studies. The studied locations lie within the Patti Formation in the southern Bida Basin. A total of 23 representative samples were selected and used for this study.

Geochemical characterisation involved analysing 20 representative samples at Acme Analytical Laboratories Limited, Vancouver, Canada, for major and trace element concentrations using ultratrace inductively coupled plasma–mass spectrometer (ICP–MS; Perkin-Elmer 6000) and inductively coupled plasma–mass spectrograph.

Table 1: *Results of semi-quantitative phase analysis (wt.%).*

Mineral	Ideal formula	S1	S6a	S7a
Quartz	SiO_2	31	14	18
Kaolinite	$Al_2Si_2O_5(OH)_4$	58	80	69
Illite–Muscovite 2M1	$K_{0.65}Al_{2.0}Al_{0.65}Si_{3.35}O_{10}(OH)_2$–$KAl_2AlSi_3O_{10}(OH)_2$	4	2	3
K-feldspar	$KAlSi_3O_8$	4	3	7
Pyrite	FeS_2	0.3	-	-
Marcasite	FeS_2	1	-	-
Anatase	TiO_2	2	1	2
Rutile	TiO_2	-	-	1
Gorceixite	$BaAl_3(PO_4)(PO_3OH)(OH)_6$	-	-	1
Total		100	100	100

Aqua regia digestion was done by weighing 0.2 g aliquot into a graphite crucible and mixing with 1.5 g $LiBO_2/Li_2B_4O_7$ fusion. The crucibles were placed in an oven and heated at 98°C for 30 minutes. The cooled bead was dissolved in 5% HNO_3 (ACS grade nitric acid diluted with demineralised water) and then calibrated standard and reagent blanks were added to sample sequences.

Geochemical analysis using ultratrace ICP–MS analysis consisting of the elements Co, Mn, Fe, U, Th, Sr, V, Ca, P, La, Cr, Mg, Ba, Ti, B, Al, Na, K, W, Sc, S, Te and Ga was carried out on the claystone samples. A second 0.5 g sample split was digested in aqua regia and analysed by ICP–MS to determine Ag, Au, As, Bi, Cu, Cd, Mo, Hg, Pb, Ni, Sb, Se, Tl and Zn. An ICP emission spectrograph (Spectro Ciros Vision) was used for the determination of the basic package consisting of the following major oxides and elements: MgO, CaO, Na_2O, K_2O, TiO_2, P_2O_5, MnO, Cr_2O_3, Ba, Ni, Sr, Zr, Y, Nb and Sc. Loss on ignition (LOI) was determined by heating a predetermined amount of sample at 950°C for 90 minutes.

Quantitative phase analysis using the Rietveld method and X-ray powder-diffraction data was carried out on three representative clay samples. The samples were pulverised and reduced to the optimum grain-size range for quantitative X-ray analysis (<10 mm) by grinding using ethanol in a vibratory McCrone Micronising Mill for 10 minutes. Step-scan X-ray powder diffraction data were collected over a 2θ range of 3–80° with CoKα radiation on a Bruker D8 Advance Bragg-Brentano diffractometer equipped with an Fe monochromator foil, 0.6 mm (0.3°) divergence slit, incident and diffracted-beam Soller slits and a LynxEye XE detector. The long fine-focus Co X-ray tube was operated at 35 kV and 40 mA using a take-off angle of 6°. The X-ray diffractograms were then analysed using the International Centre for Diffraction Database PDF-4 and Search-Match software by Bruker and refined with Rietveld program Topas 4.2 (Bruker AXS).

Results and discussion

Clay mineralogy

The mineralogy of the claystone samples was revealed by semi-quantitative phase analysis using Rietveld refinements plots (Table 1). These amounts represent the relative amounts of crystalline phases normalised to 100%. The Rietveld refinement plots are shown in Figures 3–5.

These plots revealed prominent kaolinite (average value of 66.0%) as the dominant mineral with minor amounts of quartz, illite-muscovite, K-feldspar, pyrite, marcasite, anatase, rutile and gorceixite. The relatively high proportion of kaolinite is attributable to the weathering of feldspar-rich rocks in the humid climatic

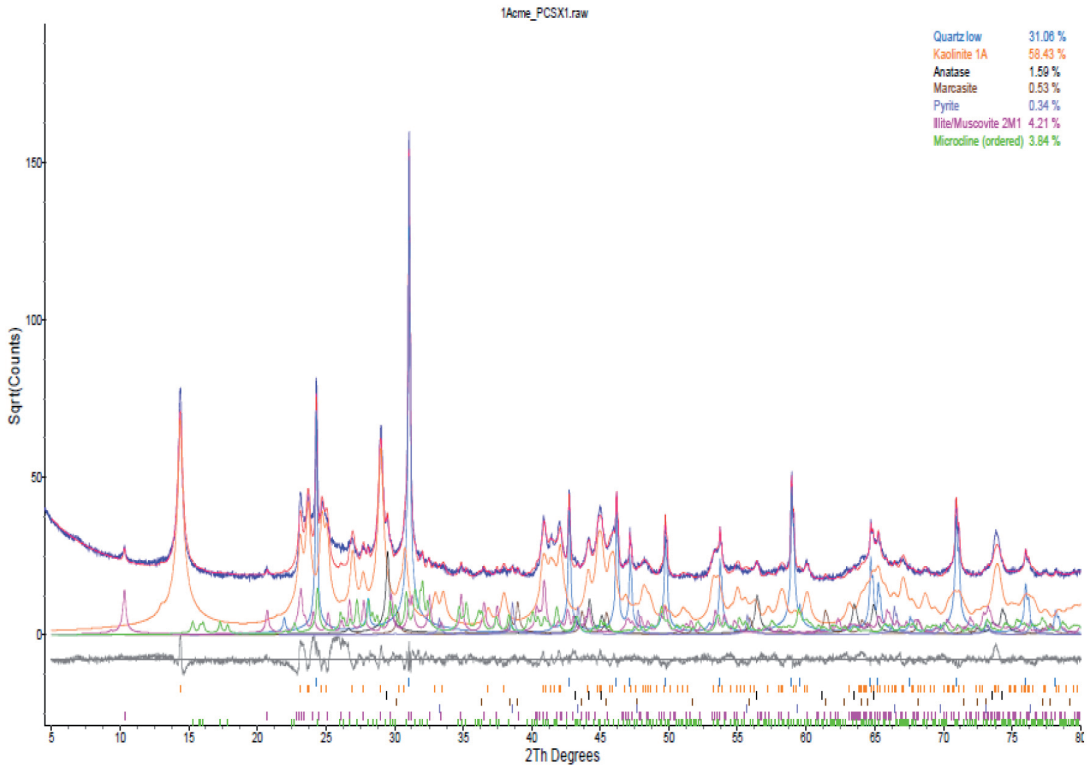

Figure 3: *X-ray diffractogram of sample S1.*

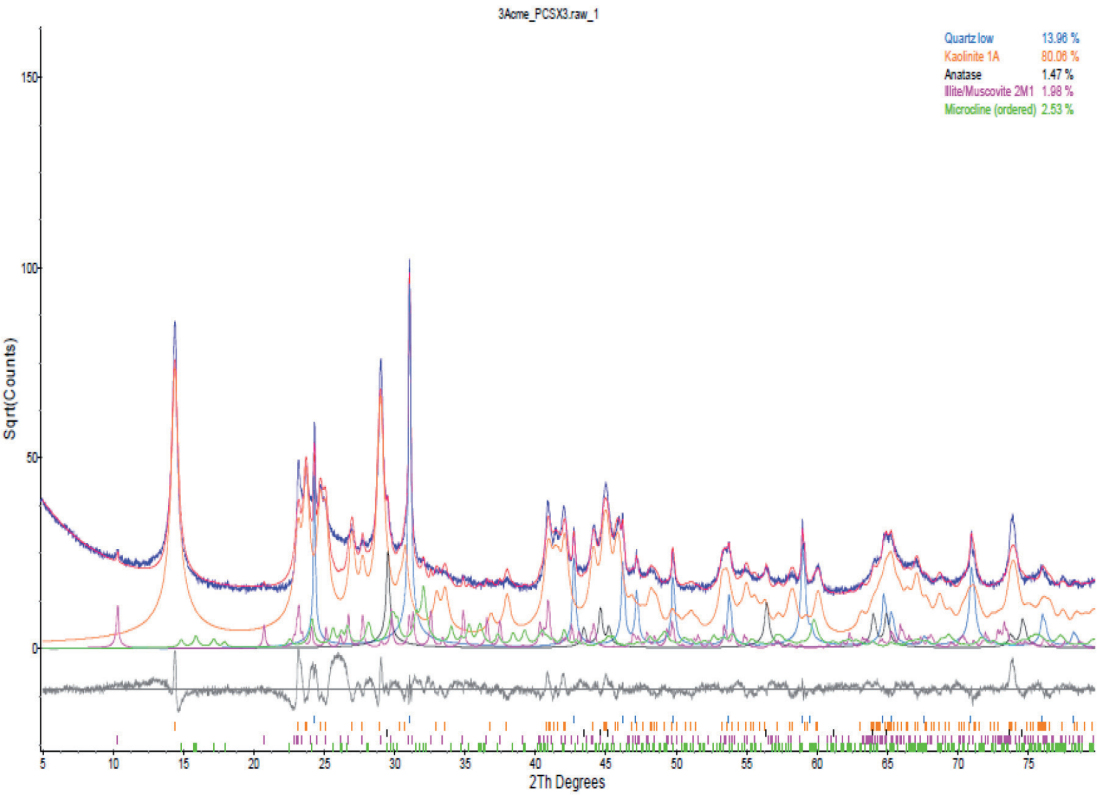

Figure 4: *X-ray diffractogram of sample S6a.*

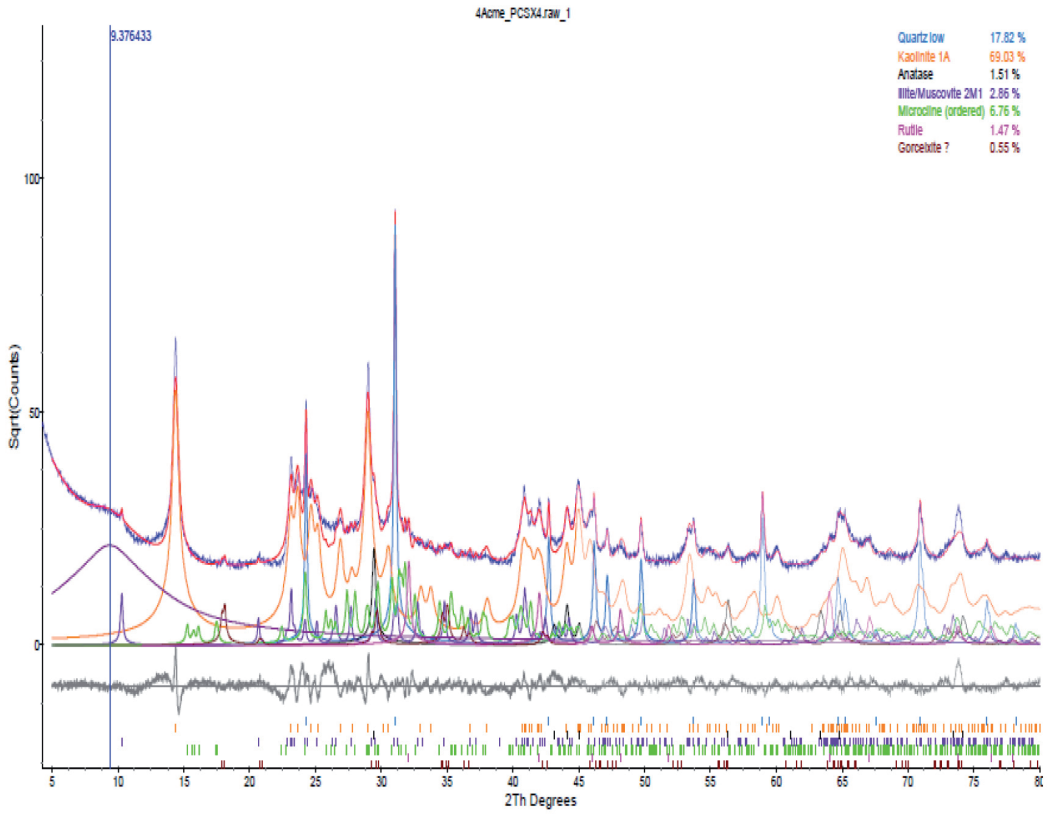

Figure 5: *X-ray diffractogram of sample S7a.*

setting [27]. The presence of kaolinite also suggests that the sediments were deposited in a continental or nearshore environment [28].

The blue lines in Figures 3–5 indicate the observed intensity at each step, red lines indicate calculated pattern, solid grey lines below indicate the difference between observed and calculated intensities and vertical bars indicate positions of all Bragg reflections. Coloured lines are the individual diffraction patterns of all phases.

Geochemistry

Major elements

Results of the major oxide analysis are summarised in Table 2. The claystones are rich in SiO_2, Al_2O_3 and Fe_2O_3 compared to K_2O, CaO, MgO, TiO_2 and Na_2O. The low concentration of K_2O (0.86%) indicates the low amount of illite or K-feldspar present [29], while the low content of CaO (0.05%) may be attributed to the absence of marine carbonate facies in the associated sedimentary sequence [30]. Low Fe_2O_3+TiO_2+MgO value (average value of 1.23%) implies that the clays are chemically inert and non-corrosive [31]; therefore, they may offer good quality kaolin.

The K_2O/Al_2O_3 ratio of sediments can be used as an indicator of the original composition of ancient sediments. According to Cox et al. [32], K_2O/Al_2O_3 ratios for clay minerals and feldspars are different with values of 0.0–0.3 and 0.3–0.9, respectively. In this study, the K_2O/Al_2O_3 ratios for the claystones vary from 0.01 to 0.06, which are close to the lower limit of the clay mineral range.

Comparison of the average chemical compositions of the investigated clay samples with other known characterised clays showed that the Abraka clay [33] has higher SiO_2 (61.92%) values but lower Al_2O_3 (20.62%) values (Tables 3). Plastic fire clay, St. Louis [34], and Isan clay [35] have lower SiO_2 and higher Fe_2O_3 values. The investigated Fe_2O_3 concentration is generally low relative to the reference samples. The present

Table 2: *Major element composition for some of the claystone samples.*

	S1	S3b	S3c	S4a	S5a	S5c	S6a	S6b	S7a	S7b	Average
SiO_2	58.89	66.29	66.91	57.38	59.15	83.95	51.06	63.53	52.75	50.13	61.00
Al_2O_3	24.48	20.39	19.88	25.83	26.25	9.34	31.70	20.86	27.49	29.54	23.57
Fe_2O_3	3.27	1.17	1.26	1.16	1.25	0.57	1.37	1.60	2.99	3.05	1.77
MgO	0.11	0.11	0.14	0.13	0.10	0.05	0.11	0.22	0.55	0.49	0.20
CaO	0.04	0.08	0.06	0.16	0.06	0.01	0.02	0.02	0.03	0.03	0.05
Na_2O	0.03	0.06	0.04	0.05	0.05	0.04	0.02	0.06	0.05	0.04	0.04
K_2O	0.48	1.30	0.80	1.11	0.43	0.31	0.40	1.26	1.33	1.23	0.86
TiO_2	1.95	2.00	2.09	1.19	1.73	1.42	1.29	2.94	1.30	1.23	1.71
P_2O_5	0.08	0.07	0.04	0.38	0.04	0.04	0.05	0.07	0.24	0.18	0.12
MnO	0.01	0.02	0.01	0.01	<0.01	0.01	<0.01	0.01	0.01	<0.01	0.01
Cr_2O_3	0.016	0.012	0.012	0.018	0.015	0.007	0.015	0.016	0.019	0.023	0.02
LOI	1.4	8.2	8.6	11.5	10.7	3.8	13.9	9.2	13.0	13.9	10.32
Sum	99.76	99.70	99.84	98.92	99.79	99.55	99.95	99.79	99.76	99.85	99.70

LOI represents loss on ignition.

Table 3: *Average major element composition of the claystones compared to published works.*

Oxides	Present study on claystone	Abraka clay [33]	Plastic fire clay, St. Louis [34]	Isan clay [35]
SiO_2	61.00	61.92	57.67	60.47
Al_2O_3	23.57	20.62	24.00	17.77
Fe_2O_3	1.77	5.00	3.23	8.18
MgO	0.20	0.71	0.30	1.26
CaO	0.05	0.02	0.70	0.47
Na_2O	0.04	0.14	0.20	0.44
K_2O	0.86	0.63	0.50	1.17
TiO_2	1.71	3.20	-	-
P_2O_5	0.12	-	0.61	-
MnO	0.01	0.11	-	0.03
H_2O	-	10.69	-	9.72

study's Al_2O_3, MgO and K_2O values are comparable to plastic fire clay's values. The average SiO_2 (61.00%) and Al_2O_3 (23.57%) chemical composition in the clay samples constitutes about 84.57% of the samples' total composition. This shows that claystones are highly siliceous.

Provenance

Gritty et al. [13] noted that the low mobility of rare earth elements during weathering, transportation, diagenesis and metamorphism makes them suitable for determining provenance and tectonic setting. The trace element

Table 4: *Trace element distribution for some of the claystones from the study area (in ppm).*

	S1	S3b	S3c	S4a	S5a	S5c	S6a	S6b	S7a	S7b
Mo	0.14	0.26	<0.01	0.39	0.11	0.12	0.05	0.06	0.06	0.06
Cu	10.04	7.94	7.63	23.44	24.29	3.11	34.51	6.04	15.06	19.74
Pb	17.34	20.21	11.72	23.31	17.91	13.11	36.99	25.83	14.05	17.67
Zn	2.8	4.7	3.6	6.2	3.3	1.0	4.7	12.4	20.7	16.2
Ni	0.4	0.4	0.6	0.7	0.6	0.4	1.0	1.3	3.3	2.6
Co	0.2	0.4	0.5	0.4	0.2	0.2	0.4	0.9	2.4	1.8
Mn	7	15	8	15	2	4	7	11	33	19
U	4.2	1.3	2.3	8.1	5.7	2.0	3.1	1.6	3.0	5.5
Th	21.2	20.5	10.8	29.8	24.0	21.0	21.3	12.7	9.3	20.8
Sr	22.6	9..0	11.0	84.7	14.6	4.8	25.4	25.1	173.5	69.4
Sb	0.07	0.02	<0.02	0.02	<0.02	<0.02	<0.02	<0.02	<0.02	<0.02
Bi	0.27	0.18	0.19	0.35	0.23	0.05	0.35	0.25	0.25	0.32
V	37	5	9	12	20	7	5	13	30	26
La	36.9	27.9	18.7	71.4	34.7	32.1	31.1	22.1	30.0	42.8
Cr	27.0	11.9	10.9	29.3	24.1	4.0	24.6	14.2	26.7	29.9
Ba	51.0	22.0	23.8	260.2	18.1	23.1	33.3	45.8	225.3	164.2
B	<20	<20	<20	<20	<20	<20	<20	<20	<20	<20
Sc	7.4	2.7	2.2	11.7	7.8	3.7	8.8	2.4	8.8	13.8
Tl	0.04	0.04	0.04	0.03	0.03	<0.02	0.11	0.03	0.09	0.11
Se	0.2	<0.1	<0.1	<0.1	<0.1	<0.1	<0.1	<0.1	<0.1	<0.1
Ga	5.2	3.1	2.7	4.9	4.4	1.3	6.0	3.4	6.8	6.7
As	1.3	<0.1	0.3	0.1	<0.1	0.2	<0.1	0.3	0.7	1.2

composition of the claystones is shown in Table 4.

Provenance can also be confirmed using Y/Ni and Cr/V ratios. McLennan et al. [36] observed that high Cr/V (>10) ratio and low Y/Ni ratio (<0.5) depict ultramafic source rocks, whereas felsic source rocks show lower Cr/V (<10) ratio and higher Y/Ni ratios (>0.5). In this study, the Cr/V ratio ranges from 0.57 to 4.92, while Y/Ni ratio ranges from 0.81 to 4.25, as shown in Table 5. This assumes a felsic source rock for the studied sections.

Furthermore, for most clastic rocks, the Al_2O_3/TiO_2 ratio is used to infer source rock composition. Al_2O_3/TiO_2 ratio ranges of 3–8 are given for mafic igneous rocks, 8–21 are given for intermediate rocks and 21–70 are given for felsic igneous rocks [9].

In this study, the Al_2O_3/TiO_2 ratio ranges from 6.57 to 24.57, suggesting intermediate to felsic igneous rocks as the probable source rocks for the claystone samples.

La/Sc and Th/Sc ratios are significantly different in felsic and basic rocks and may lead to constraints on average provenance composition [32, 37, 38]. They gave Th/Sc and La/Sc ranges between (0.84–20.5) and (2.5–16.3), respectively, for felsic source rocks. Comparison

Table 5: *Elemental ratios for some of the claystones in the study area.*

	Th/Sc	La/Sc	Y/Ni	La/Th	Cr/V	V/Cr	Ni/Co	Cu/Zn	Zr\10	U/Th
S1	2.86	4.99	2.78	1.74	0.73	1.36	2.00	3.59	120.0	0.20
S3b	7.59	1.33	3.70	1.36	2.38	0.42	1.00	1.69	186.0	0.06
S3c	4.91	8.50	2.25	1.73	1.21	0.82	1.20	2.12	71.1	0.21
S4a	2.56	6.10	3.90	2.40	2.44	0.41	1.75	3.78	135.7	0.27
S5a	3.08	4.45	2.61	1.45	1.21	0.82	3.00	7.36	88.2	0.24
S5c	5.68	8.66	4.25	1.53	0.57	1.75	2.00	3.11	312.0	0.10
S6a	2.42	3.53	0.81	1.46	4.92	0.20	2.50	7.34	31.3	0.15
S6b	5.29	9.21	2.60	1.74	1.09	0.92	1.44	0.49	71.8	0.13
S7a	1.06	3.41	1.45	3.23	0.89	1.12	1.38	0.73	28.4	0.32
S7b	1.51	3.10	1.56	2.06	1.15	0.89	1.44	1.22	24.5	0.26
Average	3.69	6.22	2.59	1.87	1.65	0.87	1.79	3.14	106.9	0.19

of La/Sc and Th/Sc ratios for the claystone samples from this study (Table 5) with this model also indicated that such ratios came within the range of felsic source rocks.

Paleo-oxygenation condition

Barnes and Cochran [39] illustrated that uranium oxidation exerts a strong influence on marine geochemistry. Low content of uranium is generally found in sediments deposited in marine environment under oxygenated conditions [40, 41], while high uranium contents are found in sediments from oxygen-depleted zones [4, 40, 42, 43]. The claystone samples show a low content of uranium (in the range of 1.3–8.1).

Cu/Zn ratio has been put forward as a redox parameter [8]. According to Hallberg [8], a high Cu/Zn ratio indicates reducing depositional conditions, while a low Cu/Zn ratio suggests oxidising conditions. In this study, the clay samples have a range of 0.49–7.36 Cu/Zn ratios (Table 5); this indicates more oxidising conditions. The U/Th ratio may be used as a redox indicator, with this ratio being higher in organic-rich mudstones [3]. The U/Th ratio below 1.25 suggests oxic deposition conditions, whereas values above 1.25 suggest suboxic and anoxic conditions [4]. In this study, the clay samples' U/Th ratio had a range of 0.06–0.32, indicating that they were deposited in an oxidising environment.

Jones and Manning [3] also suggested that Ni/Co ratios below 5 indicate oxic environments, whereas ratios above 5 indicate suboxic and anoxic environments. Thus, the low Ni/Co (1.00–3.00) ratio for the clay samples indicates that they were deposited in well-oxidising conditions.

In addition, Ernst [44], Bjorlykke [45] and Dill et al. [46] used V/Cr ratio as an index of paleo-oxygenation in various studies. Bjorlykke [45] observed that Cr is mainly incorporated in the detrital fraction of sediment and so may substitute for Al in the clay structure, whereas Shaw et al. [47] noted that V is generally found in sediments deposited in reducing environments. According to Jones and Manning [3], ratios above 2 indicate anoxic conditions, while ratios below 2 suggest oxidising conditions. In the present study, the V/Cr ratios were in the range of 0.20–1.75, which indicates that the claystones were deposited in an oxidising environment.

Tectonic setting

Bhatia and Crook [48] identified La, Th, Zr, Nb, Y, Sc, Co and Ti as being the most useful elements in discriminating different tectonic settings. Four distinct environments, oceanic island

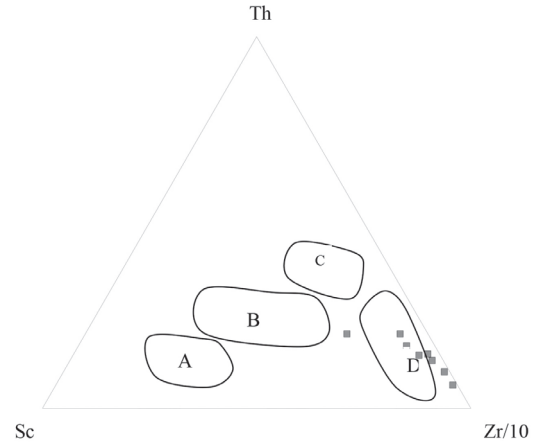

Figure 6: *Th–Sc–Zr/10 greywackes discrimination diagram [48]. The fields are as follows: A – oceanic island arc, B – continental island arc, C – active continental margin and D – passive margin.*

arc, continental island arc, active continental margin and passive margin, are recognised on La–Th–Sc and Th–Sc–Zr/10 trivariate plots. Using the Th–Sc–Zr/10 greywackes discriminant diagram of Bhatia and Crook [48], the tectonic setting for this study was adduced to be passive margin type as the claystone samples' plot was within the region specified for passive margin-type tectonic setting (Figure 6).

Passive–massive-type sandstone is generally enriched in SiO_2 and depleted in Na_2O, TiO_2 and CaO, suggesting their highly recycled and mature nature according to Bhatia [10]. The analysis of the major elements of the studied claystone samples revealed that they were also enriched in SiO_2 and depleted in Na_2O, TiO_2 and CaO (Table 3).

Conclusions

Mineralogical and geochemical analyses of the claystone samples were used to deduce compositional attributes, provenance, tectonic setting and paleo-oxygenation condition. Major element abundance showed that the claystone samples have average composition of SiO_2 (61.00%), Al_2O_3 (23.57%), Fe_2O_3 (1.77%) and TiO_2 (1.71%), constituting about 98% of the bulk chemical composition.

Mineralogical composition of the claystone sample-based Rietveld refinement plots revealed the dominant clay mineral as kaolinite with minor constituents as illite–muscovite and gorceixite. The non-clay minerals had quartz predominating with minor constituents as K-feldspar, pyrite, marcasite, anatase and rutile. The provenance indicated intermediate to felsic igneous rocks as the probable source rocks for the claystone samples. Paleo-oxygenation studies using geochemical parameters such as U, Cu/Zn, U/Th, Ni/Co and V/Cr ratios suggested that these claystones were deposited in an oxidising environment.

The tectonic setting was inferred using the Th–Sc–Zr/10 greywackes discrimination diagram [48], which distinguished the tectonic setting as passive margin type.

Acknowledgements

Profound gratitude goes to all staff of the Department of Geology, University of Ibadan, for their input towards the completion of this work. Acme Analytical Laboratories Limited, Vancouver, Canada, is also acknowledged for their role in the sample analysis.

References

[1] Gary, N. (2009): *Sedimentology and Stratigraphy*, 2nd edition, United Kingdom: Wiley Blackwell, p.21.

[2] Calvert, S.E., Pedersen, T.F. (1993): Geochemistry of Recent toxic and anoxic marine sediments, implications for the geological records. *Marine Geology*, 113(1–2), pp. 67–88.

[3] Jones, B., Manning, D.C. (1994): Comparison of geochemical indices used for the interpretation of paleo-redox conditions in Ancient mudstones. *Chemical Geology*, 11(1–4), pp. 111–129.

[4] Nath, B.N., Bau, M., Ramalingeswara, B., Rao, C.M. (1997): Trace and rare earth elemental variation in Arabian Sea sediments through a transect across the oxygen minimum zone. *Geochimica et Cosmochimica Acta*, 61(12), pp. 2375–2388.

[5] Cullers, R.L. (2002): Implications of elemental concentrations for provenance, redox conditions and metamorphic studies of shales and limestones near Pueblo, Colorado, USA. *Chemical Geology*, 19(4), pp. 305–327.

[6] Armstrong-Altrin, J.S., Verma, S.P., Madhavaraju, J., Lee, Y.I., Ramasamy, S. (2003): Geochemistry of Late

Miocene Kudankulam Limestones, South India. *International Geology Review*, 45(1), pp. 16–26.

[7] Dobrzinski, N., Bahlburg, H., Strauss, H., Zhang, Q.R. (2004): Geochemical climate proxies applied to the Neoproterozoic glacial succession on the Yangtze Platform, South China. In: Jenkins, G. *et al.* (Eds.). *American Geophysical Union Monograph Series*, 146, pp. 13–32.

[8] Hallberg, R.O. (1976): A geochemical method for investigation of palaeoredox conditions in sediments. *Ambio Special Report*, 4, pp. 139–147.

[9] Hayashi, K., Fujisawa, H., Holland, H., Ohmoto, H. (1997): Geochemistry of ~1.9Ga sedimentary rocks from north eastern Labrador, Canada. *Geochimica et Cosmochimica Acta,* 61(19), pp. 4115–4137.

[10] Bhatia, M.R. (1983): Plate tectonics and geochemical composition of sandstones. *Journal of Geology*, 91, pp. 611–627.

[11] Roser, B.P., Korsch, R.J. (1986): Determination of tectonic setting of sandstone mudstone suites using SiO_2 content and K_2O/Na_2O ratio. *Journal of Geology*, 94, pp. 635–650.

[12] Lopez de Luchi, M.E., Hoffmann, A.S., Wemmer, K., Steeken, A. (2003): Temporal constraints on the polyphase evolution of the Sierra de San Luis Preliminary report based on biotite and muscovite cooling ages. In: Calabar, N., Libraries, E., Lopez de Luchi, M.G., Ostera, Panarello, H. (Eds.). *Actas 15*th *Congreso Geologico Argentiso*, I, pp. 309–315.

[13] Gritty, G.H., Hason, A.D., Knaack, C., Johnson, D. (1994): Provenance determined by REE. In: Sc analyses of metasedimentary rocks, boy den cave roof pendant, central Sierria Neveda, Carlifornia. *Journal of sedimentary research,* 64, pp. 68–73.

[14] Whiteman, A.J. (1982): *Nigeria; Its Petroleum Geology, Resources and Potential*. London: Graham and Trotman, 399 p.

[15] Ladipo, K.O., Akande, S.O., Mucke, A. (1994): Genesis of ironstones from Middle Niger sedimentary basin, evidence form sedimentological ore microscopic and geochemical studies. *Journal of Mining and Geology*, 30, pp. 161–168.

[16] Akande, S.O., Ojo, O.J., Ladipo, K.O. (2005): *Upper Cretaceous sequences in the southern Bida Basin, Nigeria*. A field guide book (Nigerian Association of Petroleum Explorationists), 60 p.

[17] Adeleye, D.R. (1975): A fauna from the ironstones of the middle Niger valley, Nigeria. *Journal of Mining Geology*, 8, pp. 45–48.

[18] Okunlola, O.A., Olubunmi, I. (2012): The geochemistry of claystone-shale deposits from the Maastrichtian Patti formation, Southern Bida basin, Nigeria. *Earth Sciences Research Journal,* 16(2), pp. 57–67.

[19] Agyingi, C.M. (1991): *Geology of Upper Cretaceous rocks in the eastern Bida, Nigeria*. Ph.D. Thesis. Ibadan: University of Ibadan 1991; 501 p.

[20] Oyawoye, M.O. (1972): *The basement complex of Nigeria*. In: African geology, Dessauvagie, T.F.J., Whiteman, A.J. (eds.). Ibadan University Press, pp. 66–102.

[21] Adeleye, D.R., Dessauvagie, T.F.G. (1972): *Stratigraphy of the Niger embayment near Bida, Nigeria*. In: African Geology, Dessauvagie, T.F.G., Whiteman, A.J. (eds.). University of Ibadan Press, pp. 181–186.

[22] Adeleye, D.R. (1971): *Stratigraphy and sedimentation of the Upper Cretaceous strata around Bida, Nigeria*. Ph.D. Thesis. Ibadan: University of Ibadan 1971; 297 p.

[23] Akande, S.O., Ojo, O.J. (2002): Organic Petrology and Rock-Eval studies on source rock facies of Campion-Maastrichtian Patti Formation, southern Bida basin, Nigeria. *Nigerian Association of Petroleum Explorationists Bulletin,* 16, pp. 21–39.

[24] Ojo, S.B. (1984): Middle Niger Basin Revisited, Magnetic constraints on gravity interpretations. Nigerian Mining and Geosciences Society Conference, Nsukka, Nigeria, Abstract, pp. 52–53.

[25] Adelana, S.M.A., Olasehinde, P.I., Bale, R.B., Vrbka, P., Goni, I.B., Edet, A.E. (2008): *An overview of the geology and hydrogeology of Nigeria*. In: Applied Groundwater Studies in Africa. IAH Selected Papers on Hydrogeology, Adelana, S.M.A., MacDonald, A.M. (eds.). London: CRC Press Balkema,13, pp. 71–197.

[26] Fagbohun, B.J., Adeoti, B., Aladejana, O.O. (2017): Litho-structural analysis of eastern part of Ilesha schist belt, Southwestern Nigeria. *Journal of African Earth Sciences*, *133 p.* Available on: <http://doi.org/10.1016/j.jafrearsci.2017.05.017>.

[27] Nton, M.E. (1999): Sedimentology and depositional environment of Awi Formation, Calabar Flank, southeastern Nigeria*. Journal of Mining and Geology*, 35(1), pp. 23–36.

[28] David, J.W., Roger, M.S. (1977): Late Quarternary and clay-minerals distribution on the eastern continental margin of Canada. *Journal of the Geological Society of America*, 88(2), pp. 267–272.

[29] Akpokodje, E.G., Etu-Efeotor, J.O., Olorunfemi, B.N. (1991): The composition and physical properties of some ceramic and pottery clays of southeastern Nigeria. *Journal of Mining and Geology*, 27, pp. 9–15.

[30] Imeokparia, E.G., Onyeobi, T.U.S. (2007): Geochemical and depositional characteristics of Maastrichtian

shales in parts of southwestern, Nigeria. *Journal of Mining and Geology*, 43, pp. 167–174.

[31] Ojo, O.J., Suraj, A.A., Temitope, M.A., Aminat, O.A. (2011): Sedimentological and geochemical studies of Maastrichtian clays in Bida Basin, Nigeria: Implication for resource potential. *Centrepoint Journal (Science edition)*, 17(2), pp. 78–79.

[32] Cox, R., Lowe, D.R., Cullers, R.L. (1995): The influence of sediment recycling and basement composition on evolution of mudrock chemistry in the southwestern United states. *Geochimica et Cosmochimica Acta*, 59(14), pp. 2919–2940.

[33] Emofurieta, W.O., Ogundimu, T.O., Imeokparia, F.C. (1994): Mineralogical, Geochemical and Economic Appraisal of some Clay and Shale Deposits in Southwestern and Northeastern Nigeria. *Journal of Mining and Geology,* 30, pp. 151–159.

[34] Huber, J.M. (1985): *Kaolin Clays*. Huber Corporation (Clay Division), Georgia, U.S.A.

[35] Elueze, A.A., Bolarinwa, A.T. (1995): Assessment of functional application of lateritic clay bodies in Ekiti environs, Southwestern Nigeria. *Journal of Mining and Geology*, 31, pp. 79–87.

[36] McLennan, S.M., Hemming, S., McDaniel, D.K., Hanson, G.N. (1993): *Geochemical approaches to sedimentation, provenance and tectonics. Processes controlling the composition of clastic sediments.* In: *Geological Society of America Special Paper,* Johnson, M.J., Basu, A. (eds.)*,* 284, pp. 21–40.

[37] Wronkiewicz, D.J., Condie, K.C. (1990): Geochemistry and mineralogy of sediments from the Ventersdorp and Transvaal Supergroups, South Africa: Cratonic evolution during the early Proterozoic: *Geochimica et Cosmochimica Acta*, 54(2), pp. 343–354.

[38] Cullers, R.L. (1995): The controls on the major and trace element evolution of shales, siltstones and sandstones of Ordovician to Tertiary age in the Wet Mountain region, Colorado, U.S.A: *Chemical Geology,* 123(1–4), pp. 107–131.

[39] Barnes, U.C., Cochran, J.R. (1990): Uranium removal in oceanic sediments and the oceanic U balance. *Earth and Planetary Science Letters*, 97(1–2), pp. 94–101.

[40] Somayajulu, B.L.K., Yadav, D.N., Sarin, M.M. (1994): Recent sedimentary records from the Arabian Sea. *Sedimentology Proceedings of the Indian Academy of Sciences*, 103(2), pp. 315–327.

[41] Madhavaraju, J., Ramasamy, S. (1999): Rare earth elements in limestones of Kallankurichchi Formation of Ariyalur Group, Tiruchirapalli Cretaceous, Tamil Nadu. *Journal of the Geological Society of India*, 54, pp. 291–301.

[42] Klinkhammer, G.P., Palmer, M.R. (1991): Uranium in the oceans: where it goes and why? *Geochimica et Cosmochimica Acta*, 55(7), pp. 1799–1806.

[43] Sarkar, A., Battacharya, S.K., Sarin, M.M. (1993): Geochemical evidence for anoxic deep water in the Arabian Sea during the last glaciation. *Geochimica et Cosmochimica Acta*, 57(5), pp. 1009–1016.

[44] Ernst, T.W. (1970): *Geochemical facies analysis*, Amsterdam: Elsevier, 152 p.

[45] Bjorlykke, K. (1974): Geochemical and mineralogical influence of Ordovician island arcs on epicontinental clastic sedimentation: a study of Lower Paleozoic sedimentation in the Oslo region, Norway. *Sedimentology*, 21(2), pp. 251–272.

[46] Dill, H., Teshner, M., Wehner, H. (1988): Petrography, inorganic and organic geochemistry of Lower Permian Carboniferous fan sequences (Brandschiefer Series) FRG: constraints to their paleogeography and assessment of their source rock potential. *Chemical Geology*, 67(3–4), pp. 307–325.

[47] Shaw, T.J., Geiskes, J.M., Jahnk, R.A. (1990): Early diagenesis in differing depositional environments: the response of transition metals in pore water. *Geochimica et Cosmochimica Acta*, 54(5), pp. 1233–1246.

[48] Bhatia, M.R., Crook, A.W. (1986): Trace element characteristics of greywackes and tectonic setting discrimination of sedimentary basins. *Contributions to Mineralogy and Petrology,* 92, pp. 181–193.

Instructions for Authors

RMZ – MATERIALS & GEOENVIRONMENT (RMZ – Materiali in geookolje) is a periodical publication with four issues per year (established in 1952 and renamed to RMZ – M&G in 1998). The main topics are Mining and Geotechnology, Metallurgy and Materials, Geology and Geoenvironment.
RMZ – M&G publishes original scientific articles, review papers, preliminary notes, and professional papers in English. Only professional papers will exceptionally be published in Slovene. In addition, evaluations of other publications (books, monographs, etc.), in memoriam, presentation of a scientific or a professional event, short communications, professional remarks and reviews published in RMZ – M&G can be written in English or Slovene. These contributions should be short and clear.
Authors are responsible for the originality of the presented data, ideas and conclusions, as well as for the correct citation of the data adopted from other sources. The publication in RMZ – M&G obligates the authors not to publish the article anywhere else in the same form.

Specification of the Contributions

Optimal number of pages is 7 to 15; longer articles should be discussed with the Editor-in-Chief prior to submission. All contributions should be written using the ISO 80000.

- Original scientific papers represent unpublished results of original research.
- Review papers summarize previously published scientific, research and/or expertise articles on a new scientific level and can contain other cited sources which are not mainly the result of the author(s).
- Preliminary notes represent preliminary research findings, which should be published rapidly (up to 7 pages).
- Professional papers are the result of technological research achievements, application research results and information on achievements in practice and industry.
- Publication notes contain the author's opinion on newly published books, monographs, textbooks, etc. (up to 2 pages). A figure of the cover page is expected, as well as a short citation of basic data.
- In memoriam (up to 2 pages), a photo is expected.
- Discussion of papers (Comments) where only professional disagreements of the articles published in previous issues of RMZ – M&G can be discussed. Normally the source author(s) reply to the remarks in the same issue.
- Event notes in which descriptions of a scientific or a professional event are given (up to 2 pages).

Review Process

All manuscripts will be supervised shall undergo a review process. The reviewers evaluate the manuscripts and can ask the authors to change particular segments, and propose to the Editor-in-Chief the acceptability of the submitted articles. Authors are requested to identify three reviewers and may also exclude specific individuals from reviewing their manuscript. The Editor-in-Chief has the right to choose other reviewers. The name of the reviewer remains anonymous. The technical corrections will also be done and the authors can be asked to correct the missing items. The final decision on the publication of the manuscript is made by the Editor-in-Chief.

Form of the Manuscript

All papers must be submitted via the online system.
The original file of the Template is available on RMZ – Materials and Geoenvironment Home page address: **www.rmz-mg.com**.

The contribution should be submitted in Microsoft Word. Manuscript should be written in Arial font and 12 pt font with 1.5 line spacing and should contain all figures, tables and formulas. Headings should be written in Arial bold font and shuold not be numbered. Subheadings should be written in Arial italic font. The electronic version should be simple, without complex formatting, hyphenation, and underlining. For highlighting, only bold and italic types should be used.

Annexes

Annexes are images, spreadsheets, tables, and mathematical and chemical formulas. Math formulas should be included in article as editable text and not as images.
Annexes should be included in the text at the appropriate place, and they should also be submitted as a separate document, i.e. separated from the text in the article.
Annexes should be originals, made in an electronic form (Microsoft Excel, Adobe Illustrator, Inkscape, AutoCad, etc.) and in .eps, .tif or .jpg format with a resolution of at least 300 dpi.
The width of the annex should be at least 152 mm. They should be named the same as in the article (Figure 1, Table 1). The text in the annexes should be written in typeface Arial Regular (6 pt).
The title of the image (also schemes, charts and graphs) should be indicated in the description of the image.
When formatting spreadsheets and tables in text editors, tabs, and not spaces, should be used to separate columns.
Each formula should have its number written in round brackets on its right side.
References of the annexes in the text should be as follows: “Figure 1…” and not “as shown below:”. This is due to the fact that for technical reasons the annex cannot always be placed at the exact specific place in the article.

Composition of the Manuscript

Title
The title of the article should be precise, informative and not longer that 100 characters. The author should also indicate the short version of the title. The title should be written in English as well as in Slovene..

Information on the Authors
Information on the authors should include the first and last name of the authors, the address of the institution and the e-mail address of the corresponding author.

Abstract
The abstract presenting the purpose of the article and the main results and conclusions should contain no more than 180 words. It should be written in Slovene and English.

Key words
A list of up to 5 key words (3 to 5) that will be useful for indexing or searching. They should be written in Slovene and English.

Introduction

Materials and methods

Results and discussion

Conclusions

Acknowledgements

References

The references should be cited in the same order as they appear in the article. **Where possible the DOI for the reference should be included at the end of the reference.** They should be numbered in square brackets. References should be cited according SIST ISO 690:1996 standards.

Book:
[1] Reynolds, J.M. (2011). *An introduction to Applied and Environmental Geophysics*. New York: Wiley, 710 p.

Unpublished Master thesis or PhD dissertation:
[2] Trček, B. (2001): *Solute transport monitoring in the unsaturated zone of the karst aquifer by natural tracers*. Ph. D. Thesis. Ljubljana: University of Ljubljana 2001; 125 p.

Chapter in an edited book:
[3] Blindow, N., Eisenburger, D., Illich, B., Petzold, H., Richer, T. (2007): *Ground Penetrating Radar*. In: Environmental Geology: Handbook of Field Methods and Case Studies, Knödel, K., Lange, G., Voigt, H.J. (eds.). Springer: Berlin; pp. 283–335.

Journal article : Journal title should be complete and not abbreviated.
[4] Higashitani, K., Iseri, H., Okuhara, K., Hatade, S. (1995): Magnetic Effects on Zeta Potential and Diffusivity of Nonmagnetic Particles. *Journal of Colloid and Interface Science*, 172, pp. 383–388.
[5] Mcmechan, G.A, Loucks, R.G, Mescher, P.A, Xiaoxian, Z. (2002): Characterization of a coalesced, collapsed paleocave reservoir analog using GPR and well-core data. *Geophysics*, 67, pp. 1148–1158. doi: 10.1190/1.1500376

Proceedings Paper:
[6] Benac, Č., Gržančić, Ž., Šišić, S., Ružić, I. (2008): Submerged Karst Phenomena in the Kvarner Area. In: Proceedings of the 5th International ProGEO Symposium on Conservation of the Geological Heritage, Rab, Croatia, Marjanac, T (ed.). Pro GEO Croatia: Zagreb; pp. 12–13.

Electronic source:
[7] CASREACT – Chemical reactions database [online]. Chemical Abstracts Service, 2000, renewed 2/15/2000 [cited 2/25/2000]. Available on: <http://www.cas.org/casreact.html>.

Scientific articles, review papers, preliminary notes and professional papers are published in English. Only professional papers will exceptionally be published in Slovene.

Units

SI System should be used for units. Physical quantities should be written in Italics (e.g. m, l, v, T). Symbols for units should be in plain text with spaces (e.g. 10 m, 5.2 kg/s, 2 s-1, 50 kPa). All abreviations should be spelt out in full on first appearance.

Manuscript Submission

Please submit your article via RMZ-M&G Editorial Manager System. You can find it on the address:
http://edmgr.editool.com/rmzmag/default.htm

Log in as an author and submit your article.
You can follow the status of your submission in the system manager and your e-mail.

Information on RMZ – M&G

— Assistant editor
  Jože Žarn
  E-mail address: joze.zarn@ntf.uni-lj.si

— Secretary
  Vukič Nivesč
  Telephone: +386 01 47 04 610
  E-mail address: nives.vukic@ntf.uni-lj.si

These instructions are valid from April 2017.

ISSN 1408-7073